frontiers in Plant Science

TYPE Original Research
PUBLISHED 12 November 2026
DOI 10.3389/fpls.2026.1989792

Check for updates

OPEN ACCESS

EDITED BY
Rujira Dolphen,
King Mongkut's University of Technology Thonburi, Thailand

REVIEWED BY
Chao Gao,
Chinese Academy of Sciences (CAS), China
Stanislav Juráň,
Czech Academy of Sciences, Czechia

*CORRESPONDENCE
Sergiy Medinets
sermed@ceh.ac.uk
Ben Langford
benngf@ceh.ac.uk

RECEIVED 05 September 2026
REVISED 20 October 2026
ACCEPTED 27 October 2026
PUBLISHED 12 November 2026

CITATION
Medinets S, Langford B, Wang Y, Barker C, Vieno M, Marais EA, Di Marco CF and Nemitz E (2026) Humidity and light control methacrolein dry deposition to vegetation: measurements and model implications. *Front. Plant Sci.* 17:1989792. doi: 10.3389/fpls.2026.1989792

COPYRIGHT
© 2026 Medinets, Langford, Wang, Barker, Vieno, Marais, Di Marco and Nemitz. This is an open-access article distributed under the terms of the Creative Commons Attribution License (CC BY). The use, distribution or reproduction in other forums is permitted, provided the original author(s) and the copyright owner(s) are credited and that the original publication in this journal is cited, in accordance with accepted academic practice. No use, distribution or reproduction is permitted which does not comply with these terms.

Humidity and light control methacrolein dry deposition to vegetation: measurements and model implications

Sergiy Medinets[1,2]*, Ben Langford[1]*, Yuanlin Wang[1,3], Connor Barker[4], Massimo Vieno[1], Eloise A. Marais[4], Chiara F. Di Marco[1] and Eiko Nemitz[1]

[1]Atmosphere-Biosphere Interactions, UK Centre for Ecology and Hydrology, Edinburgh, United Kingdom, [2]Regional Centre for Integrated Environmental Monitoring, Odesa National I. I. Mechnikov University, Odesa, Ukraine, [3]Environmental Research Group, School of Public Health, Imperial College London, London, United Kingdom, [4]Department of Geography, University College London, London, United Kingdom

Introduction: Volatile organic compounds (VOC), especially isoprene oxidation products such as methacrolein (MACR), contribute significantly to tropospheric ozone and secondary organic aerosol (SOA) formation. While VOC emissions are well studied, their dry deposition to vegetation remains poorly understood and is often misrepresented in atmospheric models, owing to the scarcity of dry deposition data.

Methods: We conducted controlled twin-chamber experiments to quantify the dry deposition velocity (Vd) of MACR to coniferous (Scots pine, white spruce), deciduous (birch) and evergreen (English ivy) species, each in three biological replicates, under varying temperature, relative humidity (RH) and light, with concentrations measured by PTR-ToF-MS. The resulting vegetation-specific, RH- and light-dependent parameterisations were implemented in two independent chemistry-transport models, GEOS-Chem and EMEP, within the Wesely (1989) resistance-in-series scheme.

Results: MACR dry deposition was significantly higher under light, with Vd showing strong RH dependence during illuminated periods and much lower, RH-independent values in the dark. The response varied by species: conifers displayed higher deposition rates and greater RH sensitivity than the deciduous broadleaf birch. Compensation points remained near zero, consistent with active uptake involving stomatal control and/or metabolic processing of MACR within the leaves. Deposition to water was also non-negligible and stable across RH, challenging model assumptions that assign zero deposition to water bodies. In the models, the new scheme altered simulated MACR Vd by up to ~30% in GEOS-Chem and ~200% in EMEP, changing SOA by only 0.04% in GEOS-Chem and up to 12% in EMEP across the boreal and temperate forest biomes.

Discussion: MACR serves as a tractable test case: its moderate solubility and clear stomatal signal suit it to controlled-chamber quantification, whereas extending this approach to other biogenic VOC oxidation products will require overcoming bidirectional exchange, lower solubility and measurement interferences. Accurately representing VOC dry deposition is essential to better predict SOA formation, regional air quality and their policy implications. By resolving how

stomatal and non-stomatal pathways jointly govern the uptake of a reactive gas across contrasting plant functional types, this work provides a mechanistic basis for scaling leaf-level gas exchange to canopy- and ecosystem-scale deposition, linking plant physiological control of surface conductance to atmospheric composition.

KEYWORDS

air quality, deposition velocity, isoprene oxidation, methacrolein, plant uptake, dynamic chambers, laboratory fumigation, dry deposition parameterisation

1 Introduction

Volatile organic compounds (VOCs) from both biogenic and anthropogenic sources, alongside nitrogen oxides (NO and NO_2, collectively NO_x), contribute to the formation of ground-level ozone (O_3) and fine particulate matter pollution ($PM_{2.5}$) through secondary organic aerosol (SOA) formation, with adverse effects on human health, ecosystems and agriculture (Kamens et al., 1982; Brégonzio-Rozier et al., 2015; Skiba et al., 2021). Many previous studies have concentrated on quantifying VOC emissions from plant canopies and elucidating the factors that control them, resulting in substantial advancements in atmospheric chemistry modelling (Jimenez et al., 2009). In parallel, considerable effort has been directed toward estimating atmospheric lifetimes of VOCs with respect to key oxidants, such as OH, O_3 and NO_3, enabling a more comprehensive understanding of their reactivity and fate in the atmosphere. However, considerably less attention has been devoted to quantifying the dry deposition of primary and secondary VOCs to surfaces. Most models still estimate deposition rates with resistance-in-series schemes that rely on inputs obtained by extrapolating from those of SO_2 (as a proxy for a water-soluble gas with limited reactivity) and O_3 (as a proxy for an insoluble reactive gas), making uncertain assumptions about the behaviour of key VOCs (Wesely, 2007).

Several studies have highlighted the urgent need to improve VOC parameterisation in atmospheric models, noting large discrepancies between field-measured and modelled deposition rates. For example, Nguyen et al. (2015) reported that GEOS-Chem, a widely used atmospheric chemical transport model (CTM) that relies on the same Wesely (1989) resistance-in-series dry deposition scheme as most CTMs, underestimated dry deposition for most VOCs and other trace gases. Reconciling GEOS-Chem's deposition velocities with observational data led to up to a 45% reduction in the simulated surface concentrations of these gases. Similarly, Langford et al. (2010) found that above-canopy emissions of isoprene and monoterpenes were 4 and 1.8 times lower, respectively, than the default emission factors assumed for tropical forests in the widely used MEGAN biogenic emission model, underscoring the need for more measurement-based parameterization of emission factors and, separately, of deposition velocities.

Isoprene (2-methylbuta-1,3-diene) is a major biogenic VOC emitted by vegetation into the troposphere, with annual global emissions estimated at 440–660 Tg C (Guenther et al., 2006). It is one of the most abundant non-methane hydrocarbons, accounting for roughly one-third of total annual global VOC emissions from both anthropogenic and biogenic sources combined (Guenther et al., 2006). Isoprene is highly reactive in the atmosphere, with a short atmospheric lifetime (1–2 hours) due to its rapid reaction with atmospheric oxidants (Atkinson, 2000; Atkinson et al., 2006; Karl et al., 2006). As a result, it has a strong influence on tropospheric photochemistry at local, regional and global scales (Karl et al., 2004, 2006).

Under pristine environmental conditions with low NO_x concentrations, isoprene hydroperoxides (ISOPOOHs) are the dominant first-generation oxidation products (Figure 1). In contrast, under high-NO_x conditions, the major primary oxidation products are methyl vinyl ketone (MVK), methacrolein (MACR) and formaldehyde (HCHO) (Figure 1; Miyoshi et al., 1994; Sprengnether et al., 2002). The MACR/MVK production ratio is sensitive to ambient NO_x levels, being around 0.5 in polluted air ($NO_x >> 1$ ppbv) and above 1.0 in relatively clean air ($NO_x < 0.3$ ppbv). This sensitivity reflects both the NO_x-dependent fate of isoprene peroxy radicals and a shift in the relative contribution of the initiating oxidants: hydroxyl radicals (OH) initiated oxidation, which dominates in daylight, yields more MVK than MACR, whereas a greater relative contribution from O_3-initiated oxidation raises the MACR/MVK ratio (Miyoshi et al., 1994; Sprengnether et al., 2002). The ratio is further modulated by differential loss, as MVK reacts more rapidly with O_3 than MACR (Kamens et al., 1982; Pierotti et al., 1990).

MACR (and MVK) can undergo photooxidation or participate in further reactions to form a variety of oxygenated products, with yields and ratios dependent on humidity and NO_x levels, thus influencing atmospheric chemistry, O_3 production and SOA formation (Figure 1; Nguyen et al., 2016; Xing et al., 2018; Canaval et al., 2020). MACR also contributes to SOA formation via methacryloyl peroxynitrate (MPAN), which subsequently forms hydroxymethyl-methyl-α-lactone (HMML), a key isoprene-derived SOA (iSOA) precursor under high-NO_x conditions, whereas MVK does not (Nguyen et al., 2015).

Alternatively, both isoprene-derived carbonyls can be deposited onto surfaces and/or taken up by vegetation (Langford et al., 2010, 2022; Fares et al., 2015; Cappellin et al., 2019). Thus, plant canopies may act as sinks for these oxidation products, potentially reducing iSOA and O_3 formation in the atmosphere. Despite evidence of this process, a comprehensive understanding of the environmental

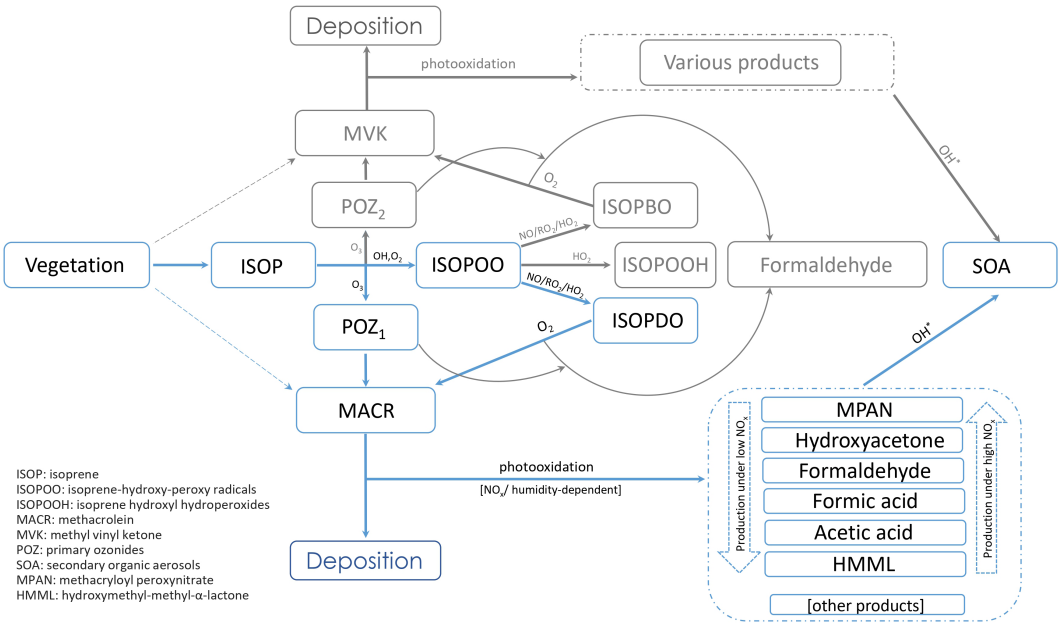

FIGURE 1
A simplified scheme of isoprene oxidation in the troposphere, showing the formation of main derivatives (isoprene hydroxy hydroperoxides, methyl vinyl ketone and methacrolein), with a focus on further chemical transformation and deposition of methacrolein (blue-highlighted section). The scheme is based on studies of Liu et al. (2013); Nguyen et al. (2015); Xing et al. (2018); Cappellin et al. (2019) and Canaval et al. (2020).

controls on carbonyl deposition is still lacking. Addressing this knowledge gap is essential for improving the performance of atmospheric models that simulate SOA and $PM_{2.5}$.

To address this gap, this study aims to:

i. conduct comprehensive measurements of MACR deposition to various plant types (coniferous, deciduous and evergreen) under controlled climate conditions across a range of temperatures, relative humidities and light/dark cycles, using a range of realistic MACR air concentrations, and to evaluate whether the observed temperature dependence of deposition velocities is consistent with the stomatal response predicted by the Wesely (1989) scheme;
ii. identify the environmental drivers that control MACR deposition velocities for the studied plant species;
iii. derive measurement-based deposition parameterisations for MACR and implement them into two independent chemical transport models, EMEP MSC-W (reduced-chemistry) and GEOS-Chem (near-explicit isoprene chemistry), to assess their impact on modelled MACR deposition rates, atmospheric MACR abundance and the subsequent formation of SOA and $PM_{2.5}$ across contrasting environments.

We hypothesize that (i) deposition velocities depend on relative humidity due to possible solubility-driven phase transfer of MACR in atmospheric water vapour or surface water films, facilitating uptake through stomata and/or surface reactions; (ii) MACR deposition velocities are higher under light than dark conditions if stomatal uptake is the dominant mechanism; (iii) the impact of isoprene-derived carbonyl uptake varies across ecosystems and climates, and should be accurately represented in atmospheric models to ensure reliable SOA and $PM_{2.5}$ simulations globally.

2 Materials and methods

2.1 Plant material and non-biological surfaces

Five-year-old saplings of Scots pine (*Pinus sylvestris*), white spruce (*Picea glauca*) and birch (*Betula* sp.), and one-year-old seedlings of English ivy (*Hedera helix*) were either grown at the UK Centre for Ecology & Hydrology (UKCEH) or purchased from local nurseries. The seedlings were cultivated in a greenhouse. Two months prior to the experiment, the studied species were transferred to a control room maintained at a temperature of 15 °C and a 12-hour daylight period, with a light source providing 650 µmol photons m^{-2} s^{-1} (Genoa, Intelligent Horticultural Solutions, UK). All plants were potted in the same commercial soil. Soil moisture content was monitored using a Theta probe ML3 (DELTA-T Devices, UK) every two days to maintain a near constant field capacity.

MACR deposition velocities were also calculated for three non-plant surfaces: (i) a laboratory dish filled with ultrapure deionized water, representing a persistently wet or aquatic interface; (ii) Parafilm, used as a proxy for a waxy surface; and (iii) an artificial plant composed of fluorinated ethylene propylene (FEP), simulating a chemically inert and non-reactive surface.

10.3389/fpls.2026.1989792

2.2 Gas exchange fumigation system and experimental layout

2.2.1 Gas exchange system with a fumigation unit

An automated, dynamic flow-through gas exchange system was designed (Supplementary Figure S1) comprising two identical chambers (40 L each): one for measurement, housing a plant, and a second, empty (reference) chamber. Each chamber was equipped with an internal fan to promote air mixing and maintain homogeneous conditions. A ¼-inch spiral outlet tube was installed to relieve overpressure while minimising flow disturbances. The fans generated sufficient turbulence to effectively minimise aerodynamic (R_a) and boundary layer (R_b) resistances. Under these conditions, the total resistance to deposition was primarily governed by canopy resistance (R_c), meaning the measured deposition velocities closely approximate surface-limited deposition velocities (V_{ds}).

Chambers were constructed with a polytetrafluoroethylene (PTFE) base and frame covered by a fluorinated ethylene propylene (FEP) bag secured with an external rubber band. They were operated in a temperature-controlled room. Air was supplied to each chamber at a rate of 7 L min^{-1} from a zero air generator (ZAG; LNI Swissgas Srl, Italy). The air exiting the chambers was pumped at a slightly lower rate to maintain minor overpressure within the chambers, thereby preventing ambient air ingress and ensuring experimental integrity. Both the inlet and outlet flow rates were controlled by mass flow controllers (MFC; Mass-Stream, Bronkhorst GmbH, Germany). The relative humidity (RH) inside the chambers was automatically regulated by blending dry air, passed through a Nafion® tubing, and humid air, passed through a humidifier system (PD-50T-12MSS, Perma Pure LLC, US), both sourced from the second zero air generator (ZAG; LNI Swissgas Srl, Italy).

The fumigation module consisted of two parts (Supplementary Figure S1). A Liquid Calibration Unit (Ionicon Analytik GmbH, Austria) was utilized to introduce a mixture of water-soluble VOCs (methanol, acetonitrile, acetaldehyde, acetone, acetic acid and MACR) diluted in ultrapure deionized H_2O (PURELAB Chorus 1, ELGA LabWater, UK; resistivity of 18.6 MΩ cm) into the fumigated air. Concurrently, a custom-made fumigation system was employed for water-insoluble VOCs (isoprene, benzene, α-pinene, toluene and xylene). Each VOC was individually pipetted into ¼″ OD (ID = 7/32″) PTFE tubing, the length of which was adjusted to achieve the desired concentration of the corresponding VOC in the gas phase. Each end of the permeation tubes was plugged using a 20 mm length of PTFE Rod. Individual tubes were placed into l stainless steel tubes (1/2″ OD, length = 20 cm), all of which were connected in parallel to blend the VOCs and introduce them into the main fumigation line. The fumigation concentrations of VOCs were automatically regulated by applying a programmed air dilution ramp to the initial concentrations, using a mass flow controller (MFC; Mass-stream, Bronkhorst GmbH, Germany).

In essence, air with the desired VOC concentrations from the fumigation unit entered the chambers, and the outgoing air was analysed in real-time using a proton transfer reaction time-of-flight mass spectrometer with quadrupole ion source (PTR-Qi-ToF-MS, Ionicon, Austria) and CO_2 probe GMP343 (Vaisala, Finland). Throughout the dynamic system, air flow was precisely controlled by MFCs (refer to Supplementary Figure S1).

2.2.2 Plant treatment scheme and experimental parameters

We tested four plant species, including coniferous, broadleaf and evergreen, each in three replicates, as well as three non-plant surfaces, including a water surface, a waxy surface and a chemically intact surface (see details in Section 2.1). Overall, eleven VOCs were selected for fumigation, including 6 water-soluble and 5 water-insoluble (see the list below). All VOCs used for fumigation were sourced from Sigma-Aldrich, US and had analytical purities of ≥ 98% (manufacturer specifications). Each experiment lasted for 4 days, including one day to observe pre-fumigation (background) emissions and three days with fumigation at 20, (17.5), 15 and 10 °C (see Supplementary Figure S2). Three levels of RH (40, 60 and 70%) were applied during both light and dark periods for all studied species, being fumigated with 4 concentrations of VOCs (derived from gas dilution by 10-, 5-, 2.5- and 0.5-fold) within each humidity level (Supplementary Figure S2). However, we faced challenges in maintaining the pre-set RH (at 40, 60 and 70%) under light conditions due to intensive plant transpiration, the rate of which varied across species. To preserve experimental integrity, we adjusted the initial setup so that RH in the reference chamber was automatically regulated based on the actual RH measured in the plant chamber, reflecting both the applied RH and additional moisture from plant transpiration. As a result, actual RH during illuminated periods ranged from 55% to 85% for white spruce, 65% to 85% for Scots pine and 40% to 75% for both birch and English ivy. All calculated fluxes were then normalized per unit one-sided leaf area, with total leaf area of each plant (m^2) measured after each experiment using a Li-3100C Area Meter (Li-Cor Inc., USA) and Easy Leaf Area app (Easlon and Bloom, 2014).

A limitation of this setup, identified during experimentation, arises from differences in leaf area among species relative to the fixed chamber volume. Species with greater leaf area transpired more under illumination, raising the actual chamber RH further above the pre-set value and, consequently, shifting the realised RH range upward relative to lower-biomass species. This coupling between leaf area, transpiration and chamber humidity means that the actual RH conditions could not be held identical across species under light. Future studies would benefit from standardising the ratio of leaf area to chamber volume, or from comparing species of comparable leaf area, to ensure that VOC deposition is captured under equivalent humidity conditions, particularly for lower-biomass species, whose deposition signal may be less well resolved in a relatively large chamber.

2.3 VOC flux and deposition velocity estimation

The PTR-Qi-ToF-MS is able to detect VOC-protonated ions or fragments at low levels with a high temporal resolution. During experiments, we operated the instrument in H_3O^+ mode with the

10.3389/fpls.2026.1989792

following settings: E/N ≈ 116 Td, a drift-pressure of 3.7 mbar, drift temperature of 80 °C and drift voltage of 805 V. The fumigated species were all detected at their protonated monoisotopic mass to charge ratios: methanol (m/z 33.0335), acetonitrile (m/z 42.0338), acetaldehyde (m/z 45.0335), acetone (m/z 59.0492), acetic acid (m/z 61.0284), MACR (m/z 71.0491), isoprene (m/z 69.0699), a-pinene (both the main fragment (m/z 81.0699) and the parent ion (m/z 137.1324)) and a carcinogenic BTX group (benzene (m/z 79.0542), toluene (m/z 93.0699) and xylene (m/z 107.0856)). However, due to the limitations of PTR-Qi-ToF-MS, which detects compounds based on their nominal mass-to-charge ratio (m/z) but lacks the resolution to differentiate structural isomers, we acknowledge that signals detected at a given m/z may represent a sum of isobaric compounds present in the sampled air, rather than exclusively the targeted compounds listed above.

VOC fluxes (F) were determined by the concentration difference between the measurement (plant) and blank (reference) chambers, multiplied by the chamber flow rate (Q) and normalised by the measured leaf area index (LAI):

$$F = \frac{Q \cdot (C_{plant} - C_{ref})}{LAI}$$

where F is the net flux (ng $m^{-2\ (leaf\ area)}$ s^{-1}), Q is the flow rate of air through the chamber (m^3 s^{-1}), C_{plant} *and* C_{ref} are the VOC concentrations measured in the plant and reference chambers, respectively (ng m^{-3}), and LAI is the total leaf area (m^2 m^{-2}) determined using a Li-3100C Area Meter (Li-Cor Inc., USA) and digital imaging processed with the Easy Leaf Area app (Heaslon). Dry leaf biomass was also obtained by drying in the oven at 80 °C overnight. Positive F values indicate emission fluxes, while negative values indicate deposition fluxes.

The deposition velocity is related to the flux by

$$F = -V_d \cdot C$$

where C is the VOC concentration measured within the plant chamber. Assuming negligible internal production and steady-state chamber conditions, V_d (mm s^{-1}; defined as a positive quantity) was derived as the negative of the slope of a linear regression of net fluxes against chamber VOC concentrations. The negative sign in the equation reflects the convention that deposition fluxes directed toward the (plant) surface are negative. This approach assumes aerodynamic (R_a) and boundary layer (R_b) resistances were minimized in chamber design, such that V_d approximates the surface-limited deposition velocity (V_{ds}), where bidirectional exchange was evident, the compensation point was estimated from the x-intercept of the flux-concentration regression, representing the ambient concentration at which net exchange approaches zero. The derived V_d is leaf-area-normalised, as used throughout the manuscript except in Section 4.1, where we compare and discuss leaf-area-normalised V_d and ground-area-scaled V_d (Table 1).

2.4 Auxiliary measurements

RH level and air temperature were continuously monitored with a HTM2500LF module (Measurement Specialties Inc., France) inside each chamber. The photosynthetically active radiation (PAR) was monitored using a PAR Energy Sensor SKE 510 (Skye Instruments, UK).

2.5 Data processing, statistical analysis and visualisation

All data processing was performed using Igor Pro 9.0 (WaveMetrics Inc.), TOFware v3.2.5 (Tofwerk AG), and base packages in R (v4.4.0). Raw high-resolution mass spectra were processed in TOFware following a standardised sequence of peak-shape refinement, mass-axis calibration using known ion peaks (e.g. NO^+ and $(C_6H_5I)H^+$), and multi-peak fitting of the averaged spectrum to resolve overlapping peaks. Peaks were then batch-fitted and integrated across the full-time series, and the resulting ion signals were converted to volume mixing ratios. For compounds included in the calibration standard, mixing ratios were derived directly from experimentally determined compound-specific sensitivities. For uncalibrated compounds, mixing ratios were calculated using the mass-dependent ion transmission efficiency of the instrument, determined from the experimentally derived transmission curve. Fluxes and deposition velocities were subsequently derived from these mixing ratios (see Section 2.3). The detection limit for MACR at m/z 71.049, taken as three times the standard deviation of the difference between the reference and empty chamber concentrations (Supplementary Figure S14), was 0.09 μg m^{-3} (≈ 31 pptv at 20 °C), 1 to 2 orders of magnitude below concentrations used in the fumigation experiments. Over this range, reference and empty chamber concentrations agreed to within a mean bias of −0.3% and a maximum absolute deviation of 0.12 μg m^{-3} across both light and dark conditions and all studied RH levels, confirming negligible wall interactions and light-induced in-chamber chemistry.

TABLE 1 The range of MACR V_d normalised by leaf area and upscaled to ground area using mean leaf area index (LAI) derived from literature for mature stands across temperate and boreal regions.

Species	V_d, mm s^{-1} (est. on leaf area)		V_d, mm s^{-1} (est. on ground area)		Leaf area index (LAI), m^2 m^{-2}		
	Light	Dark	Light	Dark	Mean	Range	References
Scots pine	1.24-1.52	0.01-0.05	3.1-3.8	0.03-0.13	2.5	1.5-3.6	Jonckheere et al., 2005; Lovynska et al., 2018
White spruce	0.23-0.59	0.08-0.15	1.84-4.72	0.64-1.20	8	6.3-10.4	Quiñonez-Piñón and Valeo, 2019; Eckrich et al., 2013
Birch	0.06-0.13	0.03-0.04	0.14-0.31	0.07-0.1	2.4	0.7-4.1	Seifried et al., 2020
English ivy	0.9-1.12	-*	4.5-5.6	-*	5	1-10	Leuzinger et al., 2011

*Dark-period V_d values for English ivy were highly variable and trended opposite to the other species (high at low RH, declining as RH rose); a reliable regression could not be defined, so these values are shown for reference but excluded from the analysis.

Because the replicate measurements within each RH bin were obtained from the same three plants per species, the flux data have a hierarchical (repeated-measures) structure. The RH-binned V_d are therefore reported as descriptive estimates of the mean response rather than as independent-sample inferences. For each estimate we report the slope standard error and R^2, and we quantify biological variability as the between-plant coefficient of variation (CV) of V_d, computed from the per-plant mean V_d across the three replicates, within each RH bin (Supplementary Table S1). This variability is smaller than the RH-driven change in V_d, so the reported RH dependence is robust to between-plant differences.

Statistical analyses, including regression modelling to assess relationships among variables and significance testing of mean differences using Student's *t*-test following assessment of normality, were conducted in R. Data visualization was also carried out using R base plotting functions.

2.6 Modelling

We implement the new humidity- and light-dependent MACR deposition parameterisations derived from our chamber experiments (Section 4.1) in two independent chemical transport models, EMEP MSC-W and GEOS-Chem. For both models, we conduct simulations for the months of January and July 2022.

2.6.1 EMEP

The EMEP Meteorological Synthesizing Centre-West (MSC-W) model (https://github.com/metno/emep-ctm) is an open-source 3-D Eulerian chemical transport model developed in support of the Convention on Long-Range Transboundary Air Pollution and widely used for both research and policy assessment (Simpson et al., 2012). We use version rv5.0, which incorporates the updated Cloud-J photolysis scheme (van Caspel et al., 2023) and the CRIv2R5Em chemical mechanism, an EMEP MSC-W adaptation of the Common Representative Intermediates (CRI) v2-R5 scheme including the updated CRI v2.2a isoprene chemistry (Ge et al., 2024). VOC concentrations are tracked using non-reactive tracers (denoted "_T"), which follow species-specific emission and loss processes without affecting O_3 production (Ge et al., 2024). Simulations use a two-domain configuration: a global outer domain at 1°×1.25° and a nested European domain (32.72 - 61.25° latitude; -15 - 40° longitude) at 0.3125° latitude × 0.25° longitude. The model has 21 terrain-following vertical layers extending from the surface (1000 hPa) to 100 hPa, with surface concentrations adjusted to a reference height of 3 m (Simpson et al., 2012). Meteorology is generated online with WRF v4.4.2 (Skamarock et al., 2019) driven by the meteorological reanalysis from the fifth-generation European Centre for Medium-Range Weather Forecasts (CCCS, 2025; Hersbach et al., 2020, 2023) atmospheric reanalysis of the global climate (ERA5) and employs grid nudging of large-scale meteorological variables, including wind components, temperature. The ERA5 dataset is generated using or contains modified Copernicus Climate Change Service information.

2.6.2 GEOS-Chem

We use GEOS-Chem (GC) v14.2.3 (https://doi.org/10.5281/zenodo.10246625) in its classic configuration, driven by fixed, offline NASA Modern Era Retrospective analysis for Research and Applications, version 2 (MERRA-2) reanalysis meteorology. The model includes 47 vertical layers from the surface to 0.01 hPa (~80 km). We use the global coarse-resolution version of GEOS-Chem at 4°×5° to test atmospheric composition changes resulting from updated representation of MACR dry deposition velocities on a global scale and to generate boundary conditions for a nested fine resolution simulation of GEOS-Chem over Europe. We use the same nested model domain and resolution as EMEP MSC-W. Boundary conditions are updated every 3 hours. The lowest model layer is centred at ~60 m and is ~130 m high. Isoprene oxidation is represented by the reduced Caltech isoprene mechanism (Bates and Jacob, 2019), coupled to the complex SOA scheme that includes mechanistic representation of irreversible SOA formation from isoprene (Marais et al., 2016) and reversible uptake using the volatility basis set scheme (Pye and Seinfeld, 2010) for monoterpenes and sesquiterpenes. Biomass burning emissions are climatological emissions from GFED4 (Giglio et al., 2013).

2.6.3 Harmonization of anthropogenic emissions

To ensure that differences in simulated MACR deposition reflect the deposition schemes and chemical mechanisms rather than differences in emission inputs, both models use consistent emissions over the nested regional European domain. Global anthropogenic emissions for all sectors from HTAP v3 (Crippa et al., 2023), for the most recent available year (2018). Speciated VOC emissions are not available in the HTAPv3 inventory and so are replaced by CEDS v2 (Hoesly et al., 2018).

Biogenic emissions are calculated using the MEGAN v2.1 model (Guenther et al., 2012). Biogenic emissions are calculated offline for dust, biogenic VOC, sea-salt and soil NO_x, and online for all other species.

2.6.4 Dry deposition scheme

In both models, dry deposition of MACR and other gas-phase species follows the Wesely (1989) resistance-in-series scheme. V_d is governed by aerodynamic (R_a), quasi-laminar boundary-layer (R_b) and surface/canopy (R_c) resistances. The surface resistance combines stomatal and non-stomatal (cuticular and ground) pathways. Stomatal resistance is parameterised as a function of solar radiation and temperature. In EMEP model, the land-cover from GLC-2000 (https://forobs.jrc.ec.europa.eu/glc2000) was used for global scale. Data derived from the CORINE system and from Stockholm Environment Institute at York (SEIY) system (www.york.ac.uk/http://www.sei-international.org/landcover) were used for the European scale, binned into 16 land types (Simpson et al., 2012). GEOS-Chem assigns deposition land types from the Olson (2001) land-cover map, binned into 11 land types with distinct deposition characteristics.

Global maps risk implying applicability to biomes that differ fundamentally from the temperate and boreal forests to which our measured species belong (Section 4.1). We have therefore restricted the presented model output to the three forest biomes that correspond to this functional and climatic setting (boreal forests, temperate conifer forests, and temperate broadleaf & mixed forests), delineated globally using the ecoregion dataset of Dinerstein et al. (2017). We note, however, that the parameterisation is implemented globally in both models; the restriction applies only to the spatial domain over which we present and interpret the results.

2.6.5 Derivation of the measurement-based MACR parameterisation

We partitioned the deposition velocity measured during light periods ($V_{d,light}$) into stomatal ($V_{d,s}$) and non-stomatal ($V_{d,ns}$) components. The non-stomatal term was assumed equal to the deposition velocity measured during the dark period ($V_{d,dark}$), so that the stomatal component under illuminated condition was obtained by subtraction, $V_{d,s} = V_{d,light} - V_{d,ns}$, at 5% RH increments. Darkening does not induce complete stomatal closure: residual nighttime conductance persists, varies among species, development stage and environmental conditions, and can reach up to ~30% of daytime values, although it is more typically a small (10-15%) fraction thereof (Caird et al., 2007; Yu et al., 2019; Kangur et al., 2021). As nighttime stomatal conductance was not measured in our experiments and is too variable to represent reliably from a single literature value, assuming ~85% nighttime stomatal closure (Caird et al., 2007), we attributed ~85% of the dark-period deposition to the non-stomatal pathway ($V_{d,ns} \approx 0.85 \times V_{d,dark}$), the residual ~15% representing the fraction still passing through partially open stomata at night. This is an assumption rather than a measurement and its sensitivity is quantified below. This partition affects only the derivation and not the measured V_d; it is also consistent with the models' treatment of nighttime deposition, which is dominated by the shared, radiation-independent non-stomatal resistance r_{lu} = 9000 s m^{-1} for coniferous and deciduous forests (Wesely, 1989).

Under our laboratory conditions that use a fan to generate turbulence within the chambers, both R_a and R_b are negligible, so the mean $V_{d,ns}$ over the studied RH range approximates the reciprocal of the nighttime canopy resistance ($R_c = 1/V_{d,ns}$). Assuming stomata are closed by around 85% at night (Caird et al., 2007), this nighttime R_c is roughly equivalent to the non-stomatal (cuticular) resistance, r_{lux}. We then substituted the measurement-based r_{lux} values into Equation (7) of Wesely (1989) to retrieve revised reactivity factors (f_0) of MACR dry deposition to Scots pine, white spruce and birch (Supplementary Table S2).

Stomatal resistance ($R_s = 1/V_{d,s}$) was then computed for each species at 5% RH increments. As chamber RH remained above 60% for the coniferous species under light due to active transpiration, an RH-dependent scaling factor for R_s was derived by normalising R_s at RH > 60% to those at 60% RH. For RH ≤ 60%, the scaling factor was set to unity (Supplementary Figure S3A). A mean conifer scaling factor, calculated as the average of Scots pine and white spruce, was then applied to correct R_s at RH > 60% following:

$$R_s = R_s \times 1376.7 \times \mathrm{RH}^{-1.762} \quad \text{(applicable for RH > 60 \%)}$$

The scaling factor is anchored at 60% RH and constrained by the conifer light-period measurements, which spanned approximately 57-87% RH (Scots pine 66-87%; white spruce 57-83%). Application of the fitted relationship above ~85% RH is therefore an extrapolation beyond the measured range; as the correction is monotonic in RH, this extrapolation can only increase the derived scaling factor further, and its effect on V_d remains smaller than that of the harmonised reactivity factor (f_0).

An analogous parameterisation was developed for birch, the only broadleaf species studied (Supplementary Figure S3B):

$$R_s = R_s \times 706.79 \times \mathrm{RH}^{-1.609} \quad \text{(applicable for RH > 60 \%)}$$

However, two considerations precluded its use for broadleaf forests generally: (i) the birch V_d (0.09 mm s^{-1}) was far lower than average values reported for other deciduous species (3.0-5.2 mm s^{-1}; Fares et al., 2015) and is therefore of uncertain representativeness; and (ii) regional and global estimates of birch-specific growing areas are lacking. Despite this, the scaling factors from both equations proved highly consistent (differing by up to 3% across the 60-100% RH range; Supplementary Figure S3), so for simplicity of model implementation we applied the conifer scaling factor to both coniferous and deciduous land cover.

We additionally estimated the uncertainty arising from variation in nighttime stomatal closure. A 15% reduction in assumed closure (i.e. 70% closure) increases the RH-dependent scaling factor by 1-3% across the 60-100% RH range and lowers the derived MACR reactivity factor (f_0) by 0.1, from 0.5 to 0.4 (-20%); a 15% increase (complete closure) has the opposite effect, decreasing the scaling factor by 1-3% and raising f_0 by 0.1, from 0.5 to 0.6 (+20%). A 15% deviation in assumed nighttime closure is therefore negligible for the RH-dependent scaling factor and produces only a moderate (± 20%) change in f_0, which is small relative to the difference between the two models' default f_0 values (0.05 in EMEP and 1.0 in GEOS-Chem) that dominates the simulated response. To test the impact of the new parameterisation, we applied a revised reactivity factor to MACR (f_0 = 0.5). alongside the RH-dependent R_s correction. The revised f0 value is less than the current GEOS-Chem value (1.0), but more than the EMEP value (0.05) and neither model explicitly accounts for RH-dependent Rs. To make results comparable, the effective Henry's law constant (H*) is harmonised across both models to 6.5 M atm^{-1} for MACR and 44 M atm^{-1} for MVK. These are the default values in GEOS-Chem. EMEP defaults to 2 M atm^{-1} for both compounds. Both models already use the same r_{lu} for coniferous and deciduous forests of 9000 s m^{-1} from Wesely (1989). Both models treat MACR and MVK as a pair, assigning them an equal reactivity factor (f_0) within each model (though f_0 differs between the two models), despite their differing solubility; the parameterisation was therefore applied to both compounds. For indicative purposes, the conifer RH-dependent parameterisation was also applied to deciduous forests, while assuming the higher absolute deposition rates reported for broadleaf species (Fares et al., 2015). We emphasise that the chamber results are not incorporated into the models as leaf-level V_d values. Only two dimensionless

quantities are transferred, the revised reactivity factor (f_0) and the RH-dependent stomatal-resistance scaling factor, which enter the existing Wesely (1989) resistance-in-series scheme as coefficients. Each model then computes surface resistance per land-cover class using its own LAI-dependent stomatal formulation and land-cover map, and aggregates to the grid cell as an area-weighted combination of the co-occurring classes; differences between coniferous and deciduous forests within the scheme arise principally from their LAI-driven stomatal terms, as the non-stomatal cuticular resistance (r_{lu} = 9000 s m^{-1}) is common to both. The simulated V_d changes therefore reflect the revised coefficients acting within each model's native canopy representation rather than any direct leaf-to-grid transfer of measured velocities.

3 Results

3.1 Pre-fumigation emission of isoprene and *m/z* 71.049 compounds

Pre-fumigation (background) emissions of VOCs were measured for each tree species at 20 °C over the course of a day prior to fumigation experiments (Supplementary Figure S4). All species emitted isoprene in low quantities, with average values ranging from nearly zero to 0.23 ± 0.01 ng m^{-2} s^{-1}, consistent with the low-to-moderate isoprene emission capacities reported for these species under unstressed conditions (e.g. Kesselmeier and Staudt, 1999; Jaakkola et al., 2024). Emissions were generally higher under light conditions and varied across the studied RH levels.

Emissions of compounds detected at *m/z* 71.049, which includes potential contributions form MACR and MVK, as well as other isobaric compounds (e.g., crotonaldehyde, 2-methylpropanal), were negligible across all species. These emissions were slightly elevated under illuminated conditions and tended to increase with rising RH (Supplementary Figure S4). Light-induced *m/z* 71.049 fluxes were 3–12 times lower than those of isoprene, with even greater variation (1.6-26-fold) observed under dark conditions. The highest background *m/z* 71.049 emissions were recorded for birch (mean range: 0.06–0.15 ng m^{-2} s^{-1}), followed by white spruce (0.02–0.07 ng m^{-2} s^{-1}) and Scots pine (0.01–0.06 ng m^{-2} s^{-1}). These low values are consistent with the expectation that unstressed plants produce minimal MACR and MVK under ambient conditions, as these compounds are primarily secondary oxidation products of isoprene rather than direct plant emissions (Park et al., 2011). In most cases, emissions varied insignificantly across RH ranges. Note: pre-fumigation emissions from English ivy were not recorded.

3.2 Experimental deposition fluxes and velocities

Deposition of MACR to both plant leaves and non-plant surfaces was observed during a series of laboratory experiments conducted at fumigated MACR concentrations ranging from 0.3 to 6 µg m^{-3}. Experiments were performed under different RH levels in both light and dark conditions (Supplementary Figure S2).

In general, the deposition rate of MACR to all studied surfaces increased with increasing fumigated concentration (Figure 2; Supplementary Figures S5–S7). We estimated the mean deposition velocity (V_d) of MACR for each plant species and non-plant surface

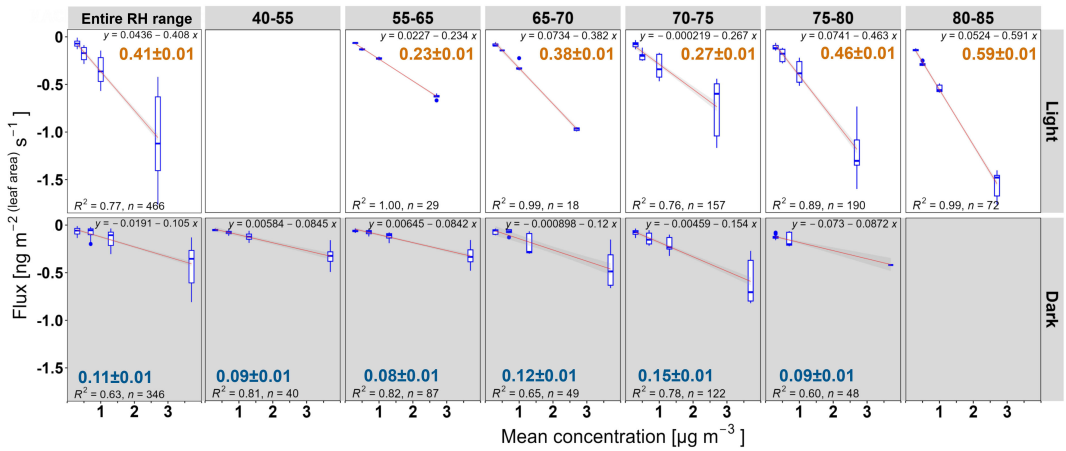

FIGURE 2
Methacrolein (MACR) deposition on spruce leaves under different relative humidity (RH, %) ranges during light and dark periods. Grey-shaded plots represent dark periods. The first vertical pair of facet plots represent the mean deposition fluxes at specific fumigated concentrations across the entire studied RH range (40-85%) under light and dark conditions. Other vertical pairs represent the mean deposition fluxes at specific fumigated concentrations under specific narrow RH ranges. Red lines show linear regressions; statistical significance was observed in all cases ($p < 0.001$). Numbers on individual plots show deposition velocities ± standard errors (mm s^{-1}; slopes of regression equations) for the entire and specific RH ranges under light (orange-highlighted values) and dark (blue-highlighted values); standard deviations in all cases were below 0.01 mm s^{-1}. All fluxes are normalised per leaf area to be comparable with other plant species studied (see Supplementary Figure S5–S7). Empty facets mean no data available for specific conditions. Boxes summarise the distribution of all replicate flux measurements (three plants x repeated measurements) at each fumigated concentration under the given RH range and light condition: the central line is the median, the box edges the interquartile range (25th-75th percentiles), and the whiskers extend to the most extreme values within 1.5x the interquartile range; points beyond the whiskers are outliers. n indicates the number of measurement points for each RH range and light condition.

across the full RH range studied, as well as within narrower RH bins, under both light and dark conditions.

During light periods, the average V_d values across the entire RH range were 1.41 mm s^{-1} for Scots pine, 0.99 mm s^{-1} for ivy, 0.41 mm s^{-1} for white spruce and 0.09 mm s^{-1} for birch during light periods (Figure 2; Supplementary Figures S5–S7). When binned into narrow RH ranges, large variations in V_d were observed (e.g., up to 256% in spruce), with a consistent tendency across all plant species for V_d to increase with rising humidity (Figure 2; Supplementary Figures S5–S7).

In contrast, during dark periods, average V_d values across the entire RH range were significantly lower: 0.04 mm s^{-1} for Scots pine, 0.11 mm s^{-1} for white spruce and 0.04 mm s^{-1} for birch. In this case, binning data into narrower RH ranges resulted in only minor variations in V_d, with no consistent RH-dependent pattern (Figure 2; Supplementary Figures S5–S7).

Among non-plant surfaces, the highest average V_d values were observed for water (0.39 and 0.46 mm s^{-1} under light and dark periods, respectively), followed by the waxy surface (0.15 mm s^{-1} under both periods), with the lowest observed for chemically resistant FEP (0.04 mm s^{-1} under both periods). Notably, RH-dependent variations in V_d were also observed for non-plant surfaces, following trends similar to those of plant species, except for water, though to a much lesser extent (Supplementary Figures S8–S10). Parameterisations derived for non-plant surfaces, including water, were not implemented in the model simulations presented here; non-plant surfaces were deliberately excluded to keep the focus on coniferous and deciduous land cover. These parameterisations are intended for incorporation and discussion in a companion study.

3.3 Modelled response to the new MACR deposition parameterisation

In GEOS-Chem, the combined lower reactivity factor and RH-dependent scaling factor produce clear spatial differences relative to the default scheme. The RH-dependent scaling factor results in an increase in MACR V_d by up to 30% in the boreal forest biome at high mid-latitudes, while the lower reactivity factor (0.5 vs default 1.0; Supplementary Table S2) causes decreases of up to 19% in the temperate conifer forest biome (Figure 3; Supplementary Figure S11). In EMEP, the new parameterisation with a higher reactivity factor (0.5 vs default 0.05; Supplementary Table S2) alongside RH-dependent scaling factor increases MACR V_d substantially across three studied biomes (boreal forest, temperate conifer forest, and temperate broadleaf & mixed forest). While the absolute increases in V_d in the boreal forest biome (0.15-0.20 cm s^{-1}) are comparable to those in GEOS-Chem (0.06-0.13 cm s^{-1}), the relative differences are more than 7 times larger in EMEP, ranging from 50 to 200% compared with 7-30% in GEOS-Chem, except for some areas of V_d decrease in the northern part of North America (Figures 3, 4; Supplementary Figures S11, S12). The low-to-moderate absolute changes (0.03-0.08 cm s^{-1}) coincide with the largest relative changes (140-200%) over temperate forests exposed to drier summers (Figure 4; Supplementary Figure S12). This pattern arises because the very low default MACR V_d in dry-summer regions makes even small absolute increases, driven by the order-of-magnitude higher reactivity factor (f_0; from 0.05 to 0.5), into large relative changes in the new EMEP parameterisation (Supplementary Table S2). The two components of the parameterisation can thus be distinguished by regime: the revised reactivity factor (f_0 = 0.5) sets the baseline response everywhere and governs it alone where RH is below 60%, including the f_0-driven decreases in the temperate conifer forest in GEOS-Chem, while the RH-dependent scaling factor adds a further increase only above 60% RH (Supplementary Figures S11, S12). Because both were derived from the same chamber measurements, they constitute a single parameterisation and are applied together.

Applying the updated MACR and MVK deposition to both models has relatively small but different effects on iSOA formation. Changes are marginal within ±0.04% in GEOS-Chem, whereas EMEP shows pronounced decreases across the studied biomes, reaching up to 11% in boreal forest regions and 12% across temperate forest regions (Figure 5). In GEOS-Chem, the updated parameterization results in decreased MACR and MVK concentration across the Eurasian boreal forests, largest part of Taiga, and the eastern North America, probably increasing the abundances of the oxidants OH, HO_2 and O_3. This in turn increases the rate of oxidation to form iSOA. Other parts of the boreal forests show a slight decrease in iSOA production, and the effect over temperate forests in only marginal.

The reduction in iSOA in EMEP is directly governed by the absolute increase in V_d of MACR and MVK across the studied biomes: faster deposition of these compounds lowers their atmospheric concentrations, reducing the pool of precursors available for iSOA formation. This results in lower iSOA, with the largest reduction across the boreal forests (Figure 5), the regions associated with the largest absolute increases in V_d (Figure 4).

Under the default schemes, the two models differ substantially in simulated MACR V_d over Europe (Supplementary Figure S13). GEOS-Chem simulates systematically higher MACR V_d than EMEP across most of the domain in both January and July 2022, due to the higher f_0 used by GEOS-Chem (1.0) compared to EMEP (0.05). The absolute difference (GEOS-Chem minus EMEP) is positive almost everywhere and largest over central and eastern Europe in summer. This inter-model spread, which exists before any modification, underscores the structural uncertainty in current VOC dry-deposition representations and provides the baseline against which our measurement-based revision should be judged. This divergence is attributable to the default reactivity factor (f_0) rather than to differences in land-cover treatment, horizontal resolution or meteorology: both the baseline inter-model spread (Supplementary Figure S13) and the revised response track f_0, whereas the non-stomatal resistance shared by the two models (r_{lu} = 9000 s m^{-1}) and the identically applied RH correction cannot generate the observed contrast.

4 Discussion

4.1 Parameterisation for RH- and light-dependent deposition velocities

In this study, we investigated the deposition rates of MACR, one of the major first-order products of isoprene oxidation in the

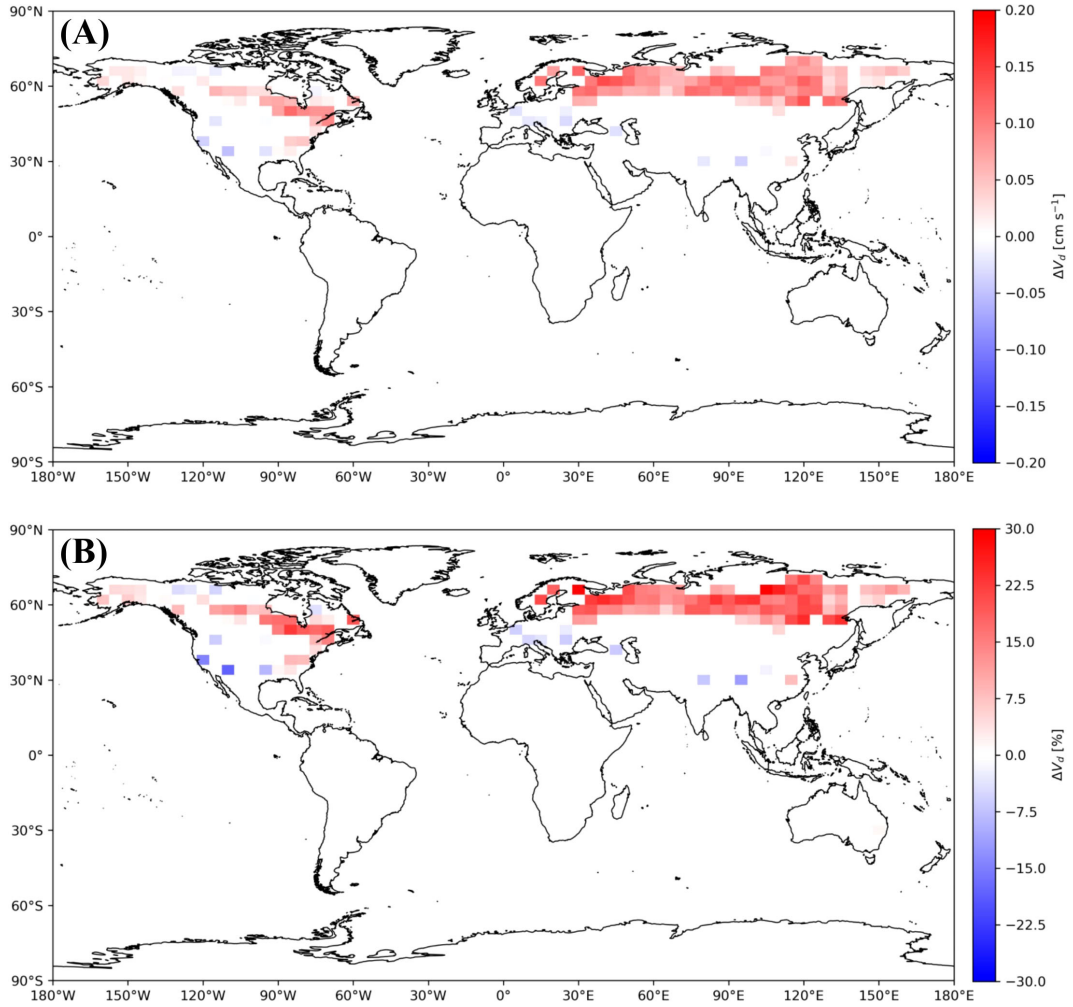

FIGURE 3
Absolute **(A)** and relative **(B)** changes in MACR deposition velocity (V_d) after applying a new measurement-based dry deposition parameterisation to GEOS-Chem. Maps are the difference in default and updated GEOS-Chem on the global coarse-resolution (4°x5°) grid for July 2022. Values are only shown for grid boxes with land fraction > 70%. Changes in V_d is shown only within boreal forests, temperate conifer forests, and temperate broadleaf & mixed forest biomes (Dinerstein et al., 2017), applied globally wherever these biomes occur; all other land and ocean areas are masked (blank).

atmosphere, and examined the environmental factor, such as ambient MACR concentration, relative humidity, temperature and light, that potentially influence MACR deposition velocities to various plant species. These included coniferous (white spruce and Scots pine), deciduous (birch) and evergreen (English ivy) species. These species collectively represent dominant and functionally distinct plant types of the boreal, temperate and Atlantic biomes of the Northern Hemisphere: Scots pine (*Pinus sylvestris*) covers approximately 145 million hectares across Northern Eurasia (Pyhäjärvi et al., 2020); white spruce (*Picea glauca*) comprises roughly a quarter of the Canadian boreal forest inventory (Soro et al., 2023); birch (*Betula* spp.) is the most important commercial broadleaved species across temperate and boreal forests of northern Europe (Hynynen et al., 2010); and English ivy (*Hedera helix*), a perennial evergreen liana native to Europe and western Asia, provides a relevant year-round surface for atmospheric deposition in temperate woodland and urban environments (Perring et al., 2020). The species were chosen to span contrasting leaf types and life forms while remaining low-to-moderate isoprene emitters, a prerequisite for isolating MACR and MVK deposition from endogenous, isoprene-derived production within the chamber; high-emitting species such as oaks were deliberately excluded on these grounds. Extension of this approach to quantitatively dominant canopy species, including Norway spruce and beech, is a priority for future work.

MACR and MVK are generally not emitted directly by plants, e.g., oak (Pierotti et al., 1990; Tani et al., 2010), which makes them particularly valuable compounds for studying dry deposition processes in vegetated environments. However, minor emissions of MACR and MVK (detected as m/z 71.049) from plant species were observed in our study (Supplementary Figure S4), consistent with previous reports from tropical forests (Karl et al., 2004), mixed beech-birch forests (Spirig et al., 2005), rainforest species (Jardine et al., 2012) and poplars (Fares et al., 2015). These findings support their endogenous production via isoprene/isoprenoid oxidation, particularly under stress conditions that generate reactive oxygen species (ROS) within leaves (Jardine et al., 2012; Niinemets et al., 2014).

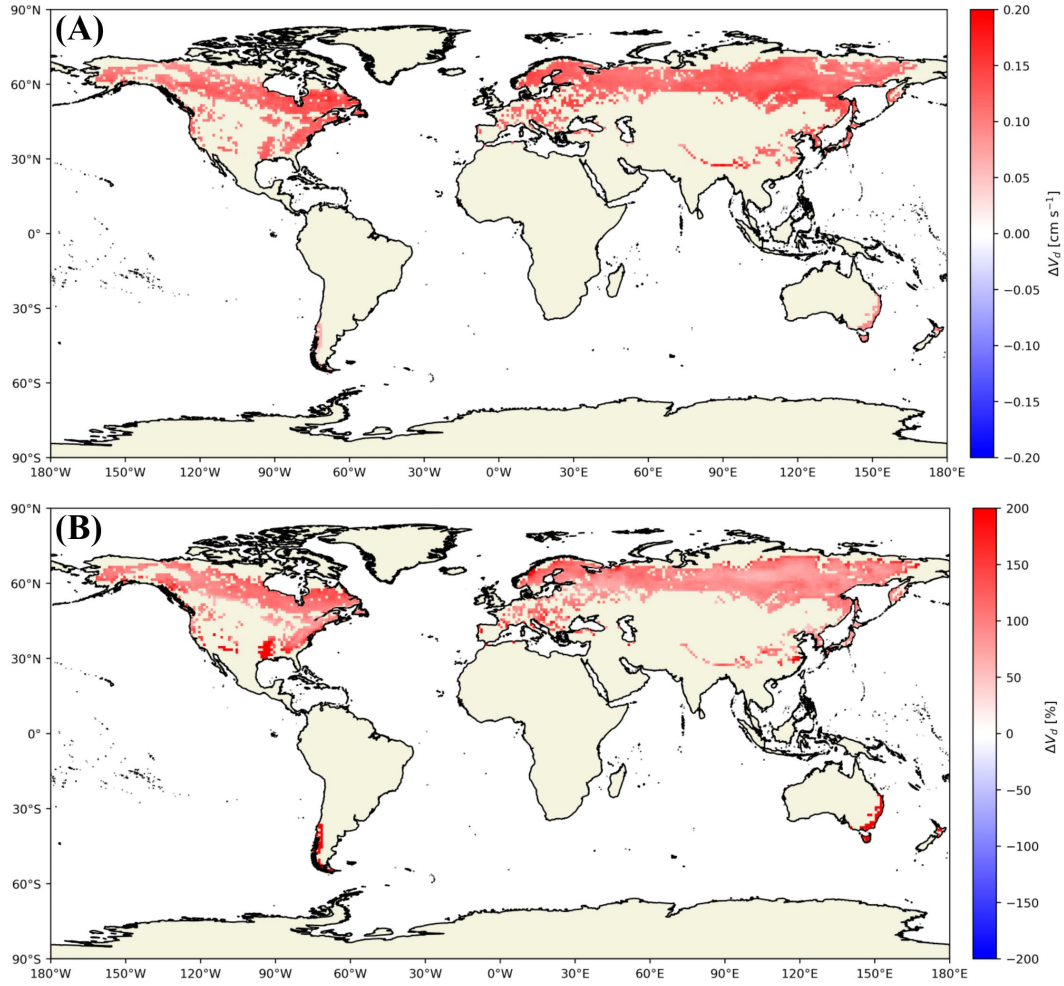

FIGURE 4
Absolute **(A)** and relative **(B)** changes in MACR deposition velocity (V_d) after applying a new measurement-based dry deposition parameterisation compared to default EMEP model performance simulated for July 2022. Land fraction > 80%. Grid cell resolution: 1°x1° (Globe) and 0.25°x0.3125° (Europe). Changes in V_d is shown only within boreal forests, temperate conifer forests, and temperate broadleaf & mixed forest biomes (Dinerstein et al., 2017), applied globally wherever these biomes occur; all other land and ocean areas are masked (blank).

As expected from the resistance-in-series framework governing dry deposition (Wesely, 1989; Nemitz et al., 2001), MACR deposition rates increased linearly with rising ambient MACR concentrations (0.3-6 μg m^{-3}; equal to 0.1-2.1 ppb at 20 °C) and were significantly higher under light conditions compared to dark periods (Figure 2; Supplementary Figures S5–S7), in agreement with previous findings (Tani et al., 2010; Fares et al., 2015). The tested concentration range is consistent with ambient MACR (+MVK) levels reported in isoprene-rich environments, which typically range from ~0.1 ppbv in boreal coniferous forests (Hakola et al., 2003) to 1–3 ppbv in temperate and tropical forests during daytime photochemical peaks (Montzka et al., 1993; Kesselmeier et al., 2002; Yáñez-Serrano et al., 2015; Liu et al., 2016), confirming the atmospheric relevance of the experimental conditions. However, lower concentrations (0.01-0.5 ppb) were often reported in areas influenced by urban/agricultural activity (Stroud et al., 2001; Worton et al., 2013; Kaltsonoudis et al., 2016). This relationship can be explained by the concentration gradient between ambient air and the internal leaf space (mesophyll and/or cuticle), driving net deposition until equilibrium (the compensation point) is reached (Conrad, 1994; Nemitz et al., 2001). The compensation point, identified as the x-intercept of the linear regression of gas flux versus concentration, was near zero for all studied species (Figure 2; Supplementary Figures S5–S7), indicating net uptake even at low ambient concentrations. The maintenance of near-zero compensation points during stepwise increases in ambient MACR concentration indicates that the effective internal MACR concentration remained low, so that deposited MACR was removed or retained faster than it re-volatilised, sustaining net uptake rather than passive accumulation. The chamber data alone do not identify the responsible sink, which could involve metabolic transformation, dissolution into surface or apoplastic water, or cuticular sorption. One well-characterised pathway consistent with this behaviour is the glutathione (GSH)-mediated intracellular metabolism identified by Muramoto et al. (2015), who showed that MACR absorption by tomato leaves exceeded partitioning theory predictions (discussed further in Section 4.3).

For the first time, we also show that MACR V_d increase with RH under light conditions (Figure 2; Supplementary Figures S5–S7). The relative increase in V_d across the studied RH ranges during

10.3389/fpls.2026.1989792

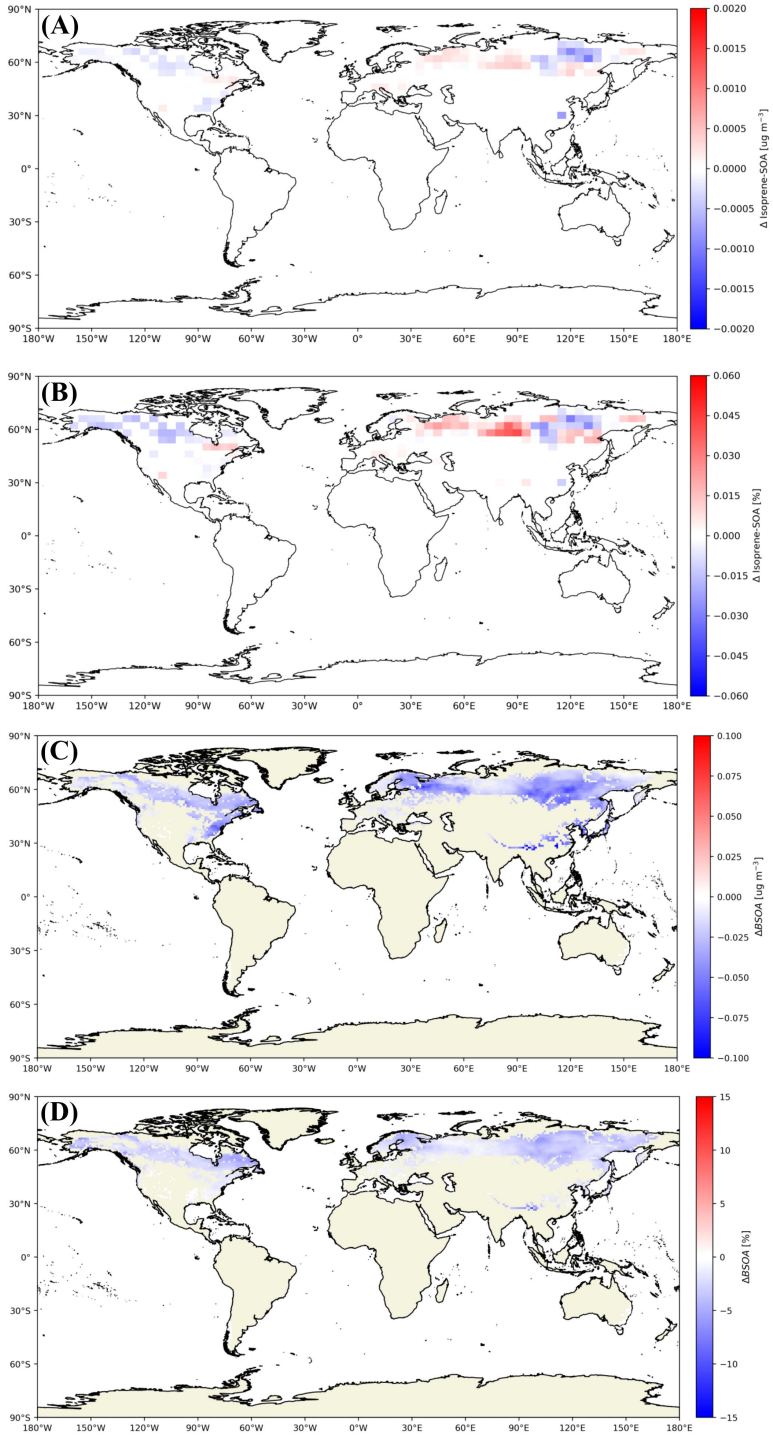

FIGURE 5
Absolute **(A, C)** and relative **(B, D)** changes in isoprene-derived SOA (iSOA) resulting from the new MACR and MVK dry deposition parameterisation relative to the default scheme, for GEOS-Chem **(A, B)** and EMEP **(C, D)**, July 2022. Note that each panel uses the same colour scheme but its own value range, so a given colour corresponds to different magnitudes between panels; the range is given on each colour bar. In GEOS-Chem, isoprene-derived SOA is calculated as the sum of aerosol-phase glyoxal, IEPOX (isoprene epoxide), low-volatility non-IEPOX product of ISOPOOH oxidation, and organonitrate hydrolysis product. In EMEP model, BSOA refers to secondary organic aerosol formed through the atmospheric oxidation of biogenic volatile organic compounds, such as isoprene and monoterpenes emitted by vegetation, followed by the partitioning of low-volatility products into the particle phase. Changes in iSOA is shown only within boreal forests, temperate conifer forests, and temperate broadleaf & mixed forest biomes (Dinerstein et al., 2017), applied globally wherever these biomes occur; all other land and ocean areas are masked (blank).

illuminated periods varied significantly by species: 157% for white spruce (Figure 2), 117% for birch (Supplementary Figure S6), 26% for English ivy (Supplementary Figure S7) and 22% for Scots pine (Supplementary Figure S5). These results highlight the importance of humidity-driven mechanisms in enhancing MACR deposition to vegetation during daylight. In contrast, no consistent RH-related trend was observed during dark periods, which were generally characterised by lower and more variable V_d values. English ivy

was the exception: its dark period V_d values were comparatively high at low RH and declined steeply as RH rose, contrary to the flat or weakly positive RH response of the other species and to ivy's own light period trend (Figure 6). Because this behaviour rested on few, widely scattered points and produced a regression of large uncertainty, a reliable dark period V_d could not be defined for ivy; these values are shown for reference (Figure 6; Table 1) but excluded from the analysis. Based on these findings, we propose a linear RH-dependent parameterization of MACR V_d (normalised per leaf area) for the studied species (Figure 6; see section 4.4). Among the conifers, Scots pine (1.24-1.52 mm s^{-1}) showed the highest V_d values under light; both needle-leaf trees showed steeper RH-V_d relationships compared to other species. Birch, a broadleaf species, had the lowest V_d values (0.06-0.13 mm s^{-1}), possibly offset by relatively higher pre-fumigation MACR emissions (0.09-0.15 ng m^{-2} s^{-1}; Figure 1), and responded least to humidity changes. In contrast, English ivy, an evergreen plant, exhibited moderate MACR V_d values (0.89-1.12 mm s^{-1}) (Figure 6). However, Fares et al. (2015) reported substantially higher leaf-scale Vd values at 30 °C under light conditions (PAR = 700 µmol m^{-2} s^{-1}) for *Paulownia imperalis* (5.2 mm s^{-1}), *Quercus ilex* (3.2 mm s^{-1}) and *Populus nigra* (3.0 mm s^{-1}). Taken together, the light requirement and RH sensitivity of MACR uptake are consistent with deposition being largely controlled by stomatal conductance, likely modulated by the hydration state of leaf surfaces, a physiological control that varies systematically among plant functional types. Resolving this leaf-level partitioning between stomatal and non-stomatal pathways is a prerequisite for representing how different vegetation types regulate the surface uptake of reactive gases, including VOCs.

While leaf-area-normalised V_d is useful for assessing species-specific MACR uptake potential and making interspecies comparisons, actual V_d values for broader applications, such as parameterising dry deposition in chemical transport models and deriving canopy-scale deposition flux estimates, should be scaled to ground area by multiplying by species-specific leaf area index (LAI) (Table 1). Actual ground-level V_d is typically higher, unless planting density is low, and depends on plant traits such as density, canopy structure and developmental stage. Also, variations in the seasonal leaf-cover duration directly affects annual uptake estimates. Among the species studied, spruce, a conifer with dense canopy, had the highest reported LAIs (~8 m^2 m^{-2}), while birch had the lowest (~2.4 m^2 m^{-2}) and a shorter vegetation season (Table 1).

We propose that this straightforward upscaling of leaf-level V_d, derived from controlled studies, to canopy-level applications is especially appropriate for MACR and MVK, as well as other VOCs predominantly formed in the atmosphere via (photo)oxidation rather than directly emitted by plants, such as hydroxyacetone, glycolaldehyde, isoprene hydroxy hydroperoxides (Supplementary Figure S3; Pierotti et al., 1990; Tani et al., 2010; Jardine et al., 2012; Fares et al., 2015; Spirig et al., 2005; Cappellin et al., 2017; Canaval et al., 2020). Reliable V_d values and parameterisations for these isoprene oxidation products are crucial for refining estimates of iSOA formation and its contribution to $PM_{2.5}$ pollution (Figure 5). Additionally, such data improve our understanding of the role of different plant types as both sources and sinks of reactive VOCs under varying environmental conditions. Moreover, integrating experimental V_d data for MACR and MVK with existing isoprene emission datasets and advanced atmospheric monitoring, including peri-urban environments, can support spatial planning decisions aimed at mitigating iSOA-related air pollution.

Our findings confirm that MACR V_d is species-specific and RH-dependent under light conditions, while at nighttime V_d is generally reduced and RH-independent (Figure 2; Supplementary Figures S5–S7; Table 1). On a ground area basis, MACR V_d under light was highest for evergreen English ivy (4.5-5.6 mm s^{-1}), followed by coniferous species (1.8-4.7 mm s^{-1}) and lowest for broadleaf Birch (0.14-0.31 mm s^{-1}). Despite these insights, both laboratory and field data for VOC dry deposition remain scarce, leading to unvalidated

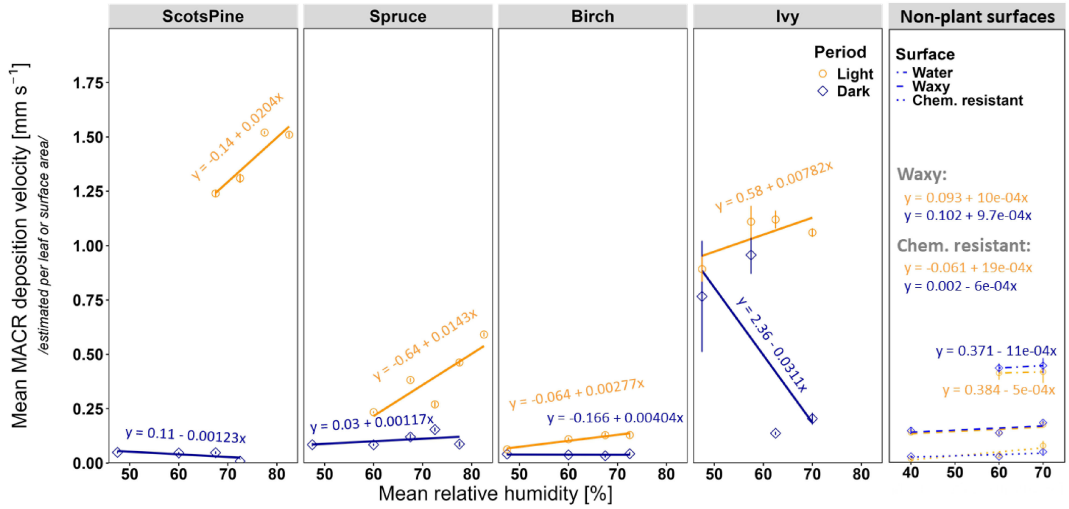

FIGURE 6
Humidity-dependent deposition velocities (V_d) of methacrolein (MACR) to the investigated coniferous (Scots pine and white spruce), deciduous (birch), evergreen (English ivy) plant species as well as non-plant surfaces, such as deionized water, waxy (parafilm) and chemical resistant (FEP) films under light and dark conditions and proposed linear regression models for parameterization. Due to a high deviation range, V_d values for ivy during the dark period are plotted for reference but were excluded from statistical analysis.

modelling assumptions. For instance, Zhang et al. (2003) used revised parameterizations based on O_3 and SO_2 to estimate uniform dry MACR V_d values (3–4 mm s^{-1}) for coniferous, deciduous and evergreen shrub vegetation. More recently, Zhang et al. (2023) used an extended version of this scheme (Wu et al., 2021) to model gridded V_d across North America using MODIS land cover data. However, they reported hourly average MACR V_d values (0.82 ± 0.96 mm s^{-1}) across all forest types, without differentiating by forest type or light conditions, making comparison with our species-specific, RH- and light-dependent data difficult.

A further challenge in accurately quantifying MACR and MVK deposition velocities, highlighted by Langford et al. (2022), is the interference from isoprene hydroxy hydroperoxides (ISOPOOH), which also register at *m/z* 71.049 and can bias continuous field measurements of the combined MVK + MACR flux. In their analysis, Langford et al. (2022) applied a single V_d of 0.45 cm s^{-1} to the MACR-MVK pair, the midpoint of the 0.3-0.6 cm s^{-1} range used for MVK and MACR in the dry deposition scheme of Zhang et al. (2003), again illustrating the reliance on uniform, non-species-specific values that our measurements are intended to refine.

Zhang et al. (2003) considered MACR and MVK deposition to water surfaces negligible, assigning a value of zero (though acknowledging true values might be non-zero, but still small at <0.4 mm s^{-1}). Our measurements indicate a measurable and stable MACR to a water surface of 0.42 ± 0.04 mm s^{-1} across a RH range of 40-70% (Supplementary Figure S8), consistent with the water-soluble nature of MACR.

Although we did not implement water-surface deposition in the model simulations presented here, this non-zero sink has potential implications for atmospheric models. Because oceans cover the majority of the Earth's surface, neglecting even a small water-surface deposition term could, in principle, lead models to overestimate how abundant MACR and MVK are and how far they are transported over remote marine regions. Over these regions, water-surface deposition likely competes with chemical loss and influences the long-range transport of these compounds and their oxidation products to downwind environments. Locally, ignoring this sink may also contribute to overestimation of iSOA and its contribution to $PM_{2.5}$. Quantifying these effects requires dedicated simulations, which we reserve for a companion study.

It is important to recognize that upscaling fluxes and V_d for other VOCs actively emitted by vegetation presents additional challenges. These compounds can undergo intra-canopy uptake or gas-phase oxidation before reaching the atmosphere, complicating the estimation of compensation points (Niinemets et al., 2014). As a result, the development of comprehensive models that incorporate advanced chemical mechanisms and bidirectional exchange processes will require further experimental and field-based research.

4.2 Exploring factors potentially impacting the results

To confirm the reliability of our findings regarding humidity-dependent deposition velocities of MACR under light conditions within the described experimental setup, we investigated several factors that could potentially influence the results and introduce bias.

4.2.1 Light radiation and in-chamber chemical reactions

MACR can undergo photooxidation in the presence of NO, forming hydroxyacetone and formaldehyde, with the production rate and yield strongly influenced by water vapour and the NO/MACR ratio (Figure 1; Xing et al., 2018). Additionally, aqueous-phase photooxidation of MACR by hydroxyl radicals (e.g., from H_2O_2) under simulated cloud conditions (Liu et al., 2009), and photooxidation in aqueous solutions containing ferric oxalate (Wang et al., 2021b), have been reported to result in the formation of secondary organic aerosols (SOA).

To assess the potential for light-induced chemical transformation of MACR in our chamber (PAR of 650 µmol photons m^{-2} s^{-1}, air residence time below 6 min), we conducted tests under purified air conditions. We observed negligible differences between (i) reference concentrations (i.e., in the entering chamber air) and actual concentrations (i.e., in the exiting chamber air), indicating an absence of significant chemical reactions within the chamber, and (ii) MACR concentrations under light versus dark conditions across the studied humidity range (Supplementary Figure S14). These results suggest that in-chamber photooxidation of MACR was negligible.

4.2.2 Temperature

Stomatal conductance, and thus gas exchange, typically increases with temperature, enhancing CO_2 uptake for photosynthesis, unless plants experience heat stress (Urban et al., 2017). Within the tested temperature range (10-20 °C), however, the effect of temperature on MACR deposition velocity varied considerably across species (Supplementary Figures S15–17; Supplementary Table S3). The two coniferous species, Scots pine and white spruce, showed a bell-shaped temperature response of V_d, with a peak near 17.5 °C (Supplementary Figures S12, S13). This pattern is qualitatively consistent with the quadratic stomatal conductance function 400/(T·(40−T)) described by Wesely (1989); Equation 3 and implemented in the GEOS-Chem model, which predicts maximum stomatal conductance near 20 °C and full stomatal closure below 0 °C and above 40 °C (Supplementary Figure S18). Importantly, our data further show that at each temperature setpoint, V_d increased with RH (Supplementary Figures S15, S16), a dependency not captured by the Wesely scheme and discussed in detail in Section 4.1. While the Wesely (1989) temperature parameterisation is widely used in chemical transport models (CTMs), several studies have identified its limitations: it omits water availability effects on stomatal conductance (Lin et al., 2019; Clifton et al., 2020) and fails to reproduce observed V_d variability during drought events (Lin et al., 2019), leading to systematic biases in modelled V_d under realistic field conditions. Furthermore, non-stomatal deposition conductance has been shown to increase on hot days, opposite to the direction predicted by the Wesely stomatal

scheme (Wong et al., 2022), highlighting that model errors in opposing pathways may partially compensate rather than consistently bias V_d estimates.

In contrast, birch (a deciduous broadleaf species) exhibited a monotonic decrease in V_d across the same temperature range (Supplementary Figure S14), a pattern inconsistent with the generic stomatal parameterisation. A similar decreasing tendency may apply to English ivy, though the limited and partly inferred nature of the ivy dataset requires this interpretation to be treated with caution. The dominance of non-stomatal (primarily cuticular) uptake pathways in this evergreen species, previously observed for hydrophilic and lipophilic compounds (Popp et al., 2005), including toluene and benzene (Yoo et al., 2006), may further complicate the temperature response of V_d for moderately soluble compounds, such as MACR (log $K_0w \approx 0.3$-0.5), as cuticular uptake is governed by different physicochemical drivers than stomatal conductance.

Overall, while these results, obtained across a narrow temperature range, are insufficient to revise temperature-dependent V_d parameterisations directly, they confirm the qualitative validity of the Wesely stomatal scheme for coniferous species and highlight the need for species-specific and vegetation-type-specific studies spanning the full biologically effective temperature range.

Consistent with a stomatal rather than a purely photosynthetic control, MACR uptake showed no correlation between MACR and CO_2 uptake fluxes (data not shown), and RH had no clear effect on CO_2 uptake (Supplementary Figures S19–S22), in line with Tani et al. (2010), who reported that MACR uptake in oak to be decoupled from both net photosynthetic and transpiration rates.

4.3 Possible mechanism involved

Absorption of MACR through stomata followed by its metabolic transformation is one likely process governing its deposition, influenced by humidity (due to the water-soluble nature of MACR) and light (through regulation of stomatal opening). Tani et al. (2010) previously reported that MACR loss due to uptake by oak trees was significantly greater than loss through reaction with OH radicals in NO_x-free air, conditions similar to those in our experimental setup.

A consistent mechanism has been proposed by Muramoto et al. (2015), who demonstrated that MACR in the vapor phase is absorbed through the stomata of tomato leaves, consistent with Henry's law, and is then rapidly metabolised via enzymatic reaction with glutathione (GSH) within the cells (Figure 7). Such pathway would account for the consistently low compensation points observed for MACR (Fares et al., 2015; this study), as no accumulation occurs in plant tissues under realistic ambient concentrations. Exogenous MACR is immediately detoxified by conjugation with GSH to form MACR-GSH, which is subsequently reduced to methallyl alcohol (MAA)-GSH within the plant cells. Spontaneous glutathionylation is therefore a plausible metabolic pathway responsible for MACR absorption (detoxification) in leaf tissues, though it has not been confirmed for the species studied here.

However, when MACR concentrations exceed the available GSH, at unrealistically high levels of five orders of magnitude greater than those found in natural environments (see Muramoto

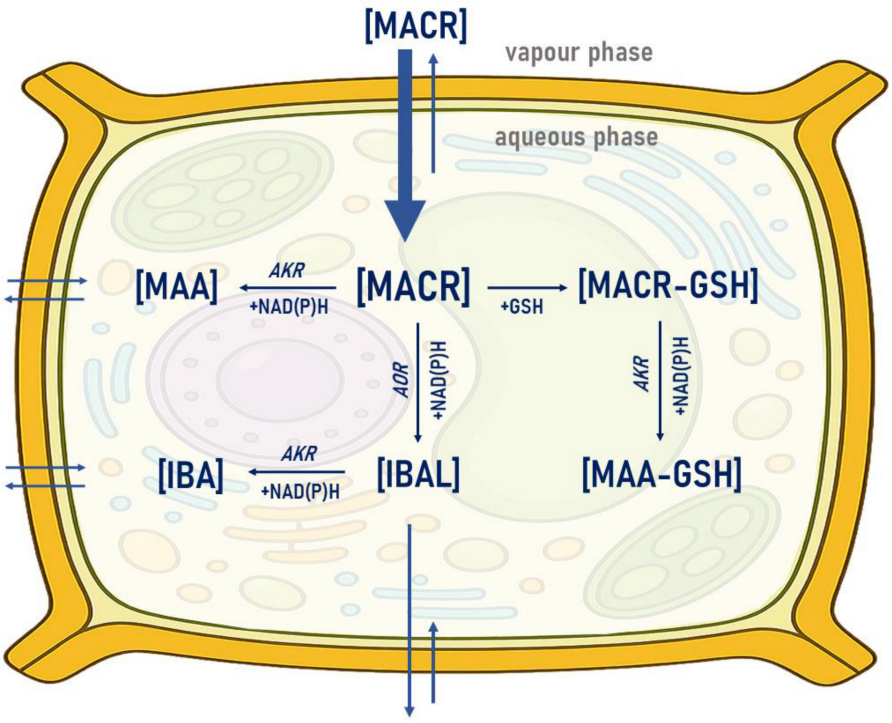

FIGURE 7
The uptake of methacrolein (MACR) from the vapour phase by plant cells and the pathways of MACR in-cell metabolism (based on Muramoto et al., 2015). GSH, glutathione; MAA, methallyl alcohol; IBAL, isobutyraldehyde; IBA, isobutyl alcohol; MACR-GSH, a glutathione conjugate of methacrolein; MAA-GSH, a glutathione conjugate of methallyl alcohol; NAD(P)H, nicotinamide adenine dinucleotide (phosphate); *AOR*, alkenal/one oxidoreductase; *AKR*, aldo-keto reductase.

et al., 2015), MACR accumulation has been shown to reduce photosynthetic capacity, similar to the effects of other reactive carbonyl species (Matsui et al., 2012; Farmer and Mueller, 2013).

Other potential mechanisms contributing to MACR uptake or transformation cannot be excluded. These include heterogeneous photochemical reactions on leaf surfaces under light conditions (Ossola and Farmer, 2024; although not yet documented for carbonyls), reactions with oxidants, such as hydroxyl radicals (Wang et al., 2021a), or interactions with *de novo* emitted VOCs (currently undocumented). However, the relevance and magnitude of these pathways remain unknown.

Additionally, leaf surface characteristics, such as moisture levels and surface area exposed to ambient MACR, likely influence observed V_d values and deposition rates. Our data show that a simulated waxy surface (parafilm) exhibited V_d values generally comparable to those of broad-leaved species such as birch (Figure 6), suggesting that waxy or resin-coated leaves may contribute significantly to overall MACR deposition. Being water-soluble, MACR deposited approximately an order of magnitude faster on a water surface (represented by deionized water) than on a dry, chemically resistant surface (represented by FEP), as shown in Figure 6. This implies that moisture films or droplets on leaf surfaces may enhance deposition. Finally, V_d of MACR to the dry, chemically resistant FEP surface was comparable to V_d observed for some species (e.g., birch and Scots pine) under dark conditions (Figure 3), indicating that physical processes (e.g., diffusion and condensation), rather than chemical or biochemical transformations, may dominate MACR deposition under such conditions.

4.4 Implications of the new measurement-based parameterisation

Our results enable revision of dry deposition mechanisms in models that share the resistance-in-series framework, but use disparate inputs. The response of both GEOS-Chem and EMEP models indicates that even a physically modest revision of the MACR surface resistance propagates into important spatially changes in V_d. The contrast between the GEOS-Chem and EMEP responses arises mainly from their use of different default reactivity factors (f_0). Harmonising f_0 to 0.5 lowers GEOS-Chem V_d where the RH correction does not compensate (dry regions), while raising EMEP V_d across the studied biomes (Figure 3, 4). As a result, the models are likely more sensitive to the updated f_0 than the inclusion of RH dependence, which applies only at RH above 60%.

The modest iSOA response in EMEP (≤12%) and relatively small in GEOS-Chem (≤0.04%) is because MACR and MVK alone are relatively minor contributors to iSOA in comparison to oxidation products ISOPOOH and IEPOX (Marais et al., 2016; Bates and Jacob, 2019). Changes in MACR removal may therefore influence SOA mainly by perturbing the local oxidant budget rather than by directly removing aerosol mass (Bates and Jacob, 2019). This indirect effect operates through altered OH and HO_x recycling and the partitioning of isoprene peroxy radicals, Both isoprene gas-phase oxidation mechanisms used here (the reduced Caltech isoprene mechanism in GEOS-Chem and the CRIv2R5/CRI v2.2a isoprene chemistry in EMEP) explicitly represent the unimolecular hydrogen-shift (1,6-H and 1,5-H) isomerisation of isoprene peroxy radicals and the associated OH regeneration (Peeters et al., 2009, 2014; Jenkin et al., 2019; Bates and Jacob, 2019). Because this OH-regenerating chemistry is active under low-NO conditions, modest changes in carbonyl sinks are expected to be largely buffered within the simulated oxidant budget, consistent with the small net iSOA effect we obtain (Figure 5).

A key limitation is that our birch-based broadleaf parameterisation is of uncertain representativeness: the measured birch V_d (Supplementary Figure S6) was roughly an order of magnitude lower than values reported for other deciduous species (Fares et al., 2015). However, the normalised scaling factor for birch coincided closely with that derived for conifers, differing by only ~3%. This consistency indicates that the normalised scaling factor is broadly reproducible across plant types, irrespective of the large differences in absolute V_d between species, supporting its use as a general basis for implementing the new parameterisation in both models; for simplicity in testing model performance, the conifer scaling factor was applied throughout. Species-specific, region-tailored measurements would nonetheless help to confirm this transferability. A second limitation is that the RH-dependent relationship is directly supported by measurements only up to ~85% RH; its use across the full 60-100% model range extrapolates the fitted power-law to the wettest conditions, where stomatal uptake is likely somewhat overestimated. Because this correction acts on the stomatal pathway above 60% RH while the non-stomatal resistance is unchanged, and because the overall model response is dominated by the harmonised reactivity factor (f_0), this extrapolation is a second-order contributor to the simulated V_d changes, but it should be constrained by high-RH field measurements in future work.

More broadly, the finding that revising a single MACR-MVK compound pair measurably alters model output motivates analogous measurement-based constraints for other reactive VOCs that are greater contributors to $PM_{2.5}$ and O_3 production and additional vegetation types. Particular priorities are compounds exhibiting bidirectional surface exchange, such as formaldehyde, formic acid and acetic acid, whose net flux switches between deposition and emission around a compensation point that varies with temperature, humidity and ambient concentration (Niinemets et al., 2014; Shutter et al., 2024). For these compounds, disentangling the concurrent and often simultaneous emission and deposition terms is essential to quantify net fluxes and to identify the environmental factors controlling them, given their importance for SOA formation and tropospheric oxidant budgets (Shutter et al., 2024).

4.5 Limitations and future directions

This study has limitations inherent to a controlled laboratory approach. Differences in leaf area relative to chamber volume produced species-specific transpiration and hence partially differing realised RH ranges under light (Section 2.2.2), so cross-species RH sensitivity is compared as the V_d-RH gradient rather than at a single fixed RH. The birch-based broadleaf parameterisation is of uncertain representativeness (Section 4.4), and our indicative extension to deciduous forests should be treated accordingly. Critically, leaf-to-canopy upscaling has not yet been validated against ecosystem-scale flux measurements. Eddy covariance fluxes, ideally combined with a fast-response instrument capable of chromatographically resolving

MACR, MVK and ISOPOOH at *m/z* 71.049 (integrating sorbent-tube GC-MS being unsuitable at eddy covariance timescales), and with concurrent O_3 and NO_x measurements, are the necessary next step, but require year-round high-frequency VOC instrumentation that remains scarce and resource-intensive. As measurement capabilities advance, field validation across a wider range of species and biomes will be essential to constrain the upscaling error and to extend the parameterisation beyond the temperate and boreal zone considered here.

5 Conclusion

This study provides the first systematic parameterisation of MACR dry deposition to diverse plant species under controlled conditions, demonstrating that MACR deposition is species-specific and strongly dependent on relative humidity and light, with significantly enhanced uptake under illumination.

Coniferous species (Scots pine and white spruce) showed the highest light- and RH-dependent deposition velocities, the broadleaf birch the lowest and the evergreen English ivy intermediate values. Near-zero compensation points and strong RH sensitivity under light point to stomatal uptake alongside surface hydration as the central controls, whereas dark deposition was minimal and RH-insensitive. Non-negligible deposition to water surfaces further suggests that models assigning zero deposition to water may overestimate atmospheric MACR and its contributions to SOA.

By resolving how stomatal and non-stomatal pathways jointly control the uptake of reactive gases (including VOCs) across contrasting plant functional types, this study links leaf-level physiological regulation of surface conductance to canopy- and ecosystem-scale deposition.

Implemented in two independent chemical transport models, the new parameterisation altered simulated MACR deposition velocities by up to ~35% in GEOS-Chem and ~200% in EMEP, while changing iSOA by only 0.1-1.0%. These results offer a measurement-based framework for improving VOC dry deposition parameterisations in regional and global air quality models and motivate species- and biome-specific deposition measurements for the broader suite of reactive, SOA-forming VOCs.

Data availability statement

The original contributions presented in the study are included in the article/Supplementary Material. Further inquiries can be directed to the corresponding authors.

Author contributions

SM: Validation, Conceptualization, Methodology, Investigation, Writing - review & editing, Formal analysis, Visualization, Data curation, Writing - original draft. BL: Formal analysis, Project administration, Writing - original draft, Data curation, Funding acquisition, Writing - review & editing, Investigation, Supervision, Validation, Conceptualization. YW: Formal analysis, Methodology, Visualization, Writing - review & editing. CB: Writing - review & editing, Visualization, Formal analysis, Methodology.

Funding

The author(s) declared that financial support was received for this work and/or its publication. This study was conducted within the UKRI/NERC-funded Dry deposition processes of volatile organic compounds (VOCDep) project (NE/V01272X/1 and NE/V012908/1) and supported by the Researcher at Risk Fellowship Program of the British Academy with the Council for At-Risk Academics (CARA).

Conflict of interest

The author(s) declared that this work was conducted in the absence of any commercial or financial relationships that could be construed as a potential conflict of interest.

Generative AI statement

The author(s) declared that generative AI was not used in the creation of this manuscript.

Any alternative text (alt text) provided alongside figures in this article has been generated by Frontiers with the support of artificial intelligence and reasonable efforts have been made to ensure accuracy, including review by the authors wherever possible. If you identify any issues, please contact us.

Publisher's note

All claims expressed in this article are solely those of the authors and do not necessarily represent those of their affiliated organizations, or those of the publisher, the editors and the reviewers. Any product that may be evaluated in this article, or claim that may be made by its manufacturer, is not guaranteed or endorsed by the publisher.

Supplementary material

The Supplementary Material for this article can be found online at: https://www.frontiersin.org/articles/10.3389/fpls.2026.1989792/full#supplementary-material

References

Atkinson, R. (2000). Atmospheric chemistry of VOCs and NOx. *Atmos. Environ.* 34, 2063–2101. doi: 10.1016/s1352-2310(99)00460-4

Atkinson, R., Baulch, D. L., Cox, R. A., Crowley, J. N., Hampson, R. F., Hynes, R. G., et al. (2006). Evaluated kinetic and photochemical data for atmospheric chemistry: Volume II–gas phase reactions of organic species. *Atmos. Chem. Phys.* 6, 3625–4055. doi: 10.5194/acp-6-3625-2006

Bates, K. H., and Jacob, D. J. (2019). A new model mechanism for atmospheric oxidation of isoprene: global effects on oxidants, nitrogen oxides, organic products, and secondary organic aerosol. *Atmos. Chem. Phys.* 19, 9613–9640. doi: 10.5194/acp-19-9613-2019

Brégonzio-Rozier, L., Siekmann, F., Giorio, C., Pangui, E., Morales, S. B., Temime-Roussel, B., et al. (2015). Gaseous products and secondary organic aerosol formation during long term oxidation of isoprene and methacrolein. *Atmos. Chem. Phys.* 15, 2953–2968. doi: 10.5194/acp-15-2953-2015

Caird, M. A., Richards, J. H., and Donovan, L. A. (2007). Nighttime stomatal conductance and transpiration in C3 and C4 plants. *Plant Physiol.* 143, 4–10. doi: 10.1104/pp.106.092940

Canaval, E., Millet, D. B., Zimmer, I., Nosenko, T., Georgii, E., Partoll, E. M., et al. (2020). Rapid conversion of isoprene photooxidation products in terrestrial plants. *Commun. Earth Environ.* 1, 44. doi: 10.1038/s43247-020-00041-2

Cappellin, L., Algarra Alarcon, A., Herdlinger-Blatt, I., Sanchez, J., Biasioli, F., Martin, S. T., et al. (2017). Field observations of volatile organic compound (VOC) exchange in red oaks. *Atmos. Chem. Phys.* 17, 4189–4207. doi: 10.5194/acp-17-4189-2017

Cappellin, L., Loreto, F., Biasioli, F., Pastore, P., and McKinney, K. (2019). A mechanism for biogenic production and emission of MEK from MVK decoupled from isoprene biosynthesis. *Atmos. Chem. Phys.* 19, 3125–3135. doi: 10.5194/acp-19-3125-2019

CCCS (2025). ERA5 Hourly Time-Series Data on Single Levels From 1940 to Present (Copernicus Climate Change Service (C3S) Climate Data Store (CDS)). Available online at: https://cds.climate.copernicus.eu/datasets/reanalysis-era5-single-levels-timeseries (Accessed 20-Jul-2026).

Clifton, O. E., Fiore, A. M., Massman, W. J., Baublitz, C. B., Coyle, M., Emberson, L., et al. (2020). Dry deposition of ozone over land: processes, measurement, and modeling. *Rev. Geophys.* 58, e2019RG000670. doi: 10.1029/2019rg000670

Conrad, R. (1994). Compensation concentration as critical variable for regulating the flux of trace gases between soil and atmosphere. *Biogeochemistry* 27, 155–170. doi: 10.1007/bf00000582

Crippa, M., Guizzardi, D., Butler, T., Keating, T., Wu, R., Kaminski, J., et al. (2023). The HTAP_v3 emission mosaic: merging regional and global monthly emissions, (2000–2018) to support air quality modelling and policies. *Earth Syst. Sci. Data* 15, 2667–2694. doi: 10.5194/essd-15-2667-2023

Dinerstein, E., Olson, D., Joshi, A., Vynne, C., Burgess, N. D., Wikramanayake, E., et al. (2017). An ecoregion-based approach to protecting half the terrestrial realm. *BioScience* 67, 534–545. doi: 10.1093/biosci/bix014

Easlon, H. M., and Bloom, A. J. (2014). Easy Leaf Area: Automated digital image analysis for rapid and accurate measurement of leaf area. *Appl. Plant Sci.* 2, 1400033. doi: 10.3732/apps.1400033

Eckrich, C. A., Flaherty, E. A., and Ben-David, M. (2013). Estimating leaf area index in Southeast Alaska: A comparison of two techniques. *PloS One* 8, e77642. doi: 10.1371/journal.pone.0077642

Farmer, E. E., and Mueller, M. J. (2013). ROS-mediated lipid peroxidation and RES-activated signaling. *Annu. Rev. Plant Biol.* 64, 429–450. doi: 10.1146/annurev-arplant-050312-120132

Fares, S., Paoletti, E., Loreto, F., and Brilli, F. (2015). Bidirectional flux of methyl vinyl ketone and methacrolein in trees with different isoprenoid emission under realistic ambient concentrations. *Environ. Sci. Technol.* 49, 7735–7742. doi: 10.1021/acs.est.5b00673

Farmer, E. E., and Mueller, M. J. (2013). ROS-mediated lipid peroxidation and RES-activated signaling. *Annu. Rev. Plant Biol.* 64, 429–450. doi: 10.1146/annurev-arplant-050312-120132

Ge, Y., Solberg, S., Heal, M., Reimann, S., van Caspel, W., Hellack, B., et al. (2024). Evaluation of modelled versus observed NMVOC compounds at EMEP sites in Europe. *EGUsphere* 2024, 1–73. doi: 10.5194/egusphere-2023-3102

Giglio, L., Randerson, J. T., and Van Der Werf, G. R. (2013). Analysis of daily, monthly, and annual burned area using the fourth-generation global fire emissions database (GFED4). *J. Geophysical Research: Biogeosciences* 118, 317–344. doi: 10.1002/jgrg.20042

Guenther, A. B., Jiang, X., Heald, C. L., Sakulyanontvittaya, T., Duhl, T., Emmons, L. K., et al (2012). The Model of Emissions of Gases and Aerosols from Nature version 2.1 (MEGAN2.1): an extended and updated framework for modeling biogenic emissions. *Geosci. Model Dev.* 5, 1471–1492. doi: 10.5194/gmd-5-1471-2012

Guenther, A., Karl, T., Harley, P., Wiedinmyer, C., Palmer, P. I., and Geron, C. (2006). Estimates of global terrestrial isoprene emissions using MEGAN (Model of Emissions of Gases and Aerosols from Nature). *Atmos. Chem. Phys.* 6, 3181–3210. doi: 10.5194/acp-6-3181-2006

Hakola, H., Tarvainen, V., Laurila, T., Hiltunen, V., Hellén, H., and Keronen, P. (2003). Seasonal variation of VOC concentrations above a boreal coniferous forest. *Atmos. Environ.* 37, 1623–1634. doi: 10.1016/s1352-2310(03)00014-1

Hersbach, H., Bell, B., Berrisford, P., Biavati, G., Horányi, A., Muñoz Sabater, J., et al. (2023). *ERA5 Hourly Data on Single Levels From 1940 to Present* (Copernicus Climate Change Service (C3S) Climate Data Store (CDS)). doi: 10.24381/cds.adbb2d47

Hersbach, H., Bell, B., Berrisford, P., Hirahara, S., Horányi, A., Muñoz-Sabater, J., et al. (2020). The ERA5 global reanalysis. *Q. J. R. Meteorol. Soc* 146, 1999–2049. doi: 10.1002/qj.3803

Hoesly, R. M., Smith, S. J., Feng, L., Klimont, Z., Janssens-Maenhout, G., Pitkanen, T., et al. (2018). Historical, (1750–2014) anthropogenic emissions of reactive gases and aerosols from the Community Emissions Data System (CEDS). *Geosci. Model. Dev.* 11, 369–408. doi: 10.5194/gmd-11-369-2018

Hynynen, J., Niemistö, P., Viherä-Aarnio, A., Brunner, A., Hein, S., and Velling, P. (2010). Silviculture of birch (Betula pendula Roth and Betula pubescens Ehrh.) in northern Europe. *Forestry* 83, 103–119. doi: 10.1093/forestry/cpp035

Jaakkola, E., Hellén, H., Olin, S., Pleijel, H., Tykkä, T., and Holst, T. (2024). Ozone stress response of leaf BVOC emission and photosynthesis in mountain birch (Betula pubescens spp. czerepanovii) depends on leaf age. *Plant-Environ. Interact.* 5, e10134. doi: 10.1002/pei3.10134

Jardine, K. J., Monson, R. K., Abrell, L., Saleska, S. R., Arneth, A., Jardine, A., et al. (2012). Within-plant isoprene oxidation confirmed by direct emissions of oxidation products methyl vinyl ketone and methacrolein. *Global Change Biol.* 18, 973–984. doi: 10.1111/j.1365-2486.2011.02610.x

Jenkin, M. E., Khan, M. A. H., Shallcross, D. E., Bergström, R., Simpson, D., Murphy, K. L. C., et al. (2019). The CRI v2. 2 reduced degradation scheme for isoprene. *Atmos. Environ.* 212, 172–182. doi: 10.1016/j.atmosenv.2019.05.055

Jimenez, J. L., Canagaratna, M. R., Donahue, N. M., Prevot, A. S. H., Zhang, Q., Kroll, J. H., et al. (2009). Evolution of organic aerosols in the atmosphere. *Science* 326, 1525–1529. doi: 10.1126/science.1180353

Jonckheere, I., Muys, B., and Coppin, P. (2005). Allometry and evaluation of in situ optical LAI determination in Scots pine: A case study in Belgium. *Tree Physiol.* 25, 723–732. doi: 10.1093/treephys/25.6.723

Kaltsonoudis, C., Kostenidou, E., Florou, K., Psichoudaki, M., and Pandis, S. N. (2016). Temporal variability and sources of VOCs in urban areas of the eastern Mediterranean. *Atmos. Chem. Phys.* 16, 14825–14842. doi: 10.5194/acp-16-14825-2016

Kamens, R. M., Gery, M. W., Jeffries, H. E., Jackson, M., and Cole, E. I. (1982). Ozone–isoprene reactions: Product formation and aerosol potential. *Int. J. Chem. Kinet.* 14, 955–965. doi: 10.1002/kin.550140902

Kangur, O., Steppe, K., Schreel, J. D., von der Crone, J. S., and Sellin, A. (2021). Variation in nocturnal stomatal conductance and development of predawn disequilibrium between soil and leaf water potentials in nine temperate deciduous tree species. *Funct. Plant Biol.* 48, 483–492. doi: 10.1071/fp20091

Karl, M., Dorn, H. P., Holland, F., Koppmann, R., Poppe, D., Rupp, L., et al. (2006). Product study of the reaction of OH radicals with isoprene in the atmosphere simulation chamber SAPHIR. *J. Atmos. Chem.* 55, 167–187. doi: 10.1007/s10874-006-9034-x

Karl, T., Potosnak, M., Guenther, A., Clark, D., Walker, J., Herrick, J. D., et al. (2004). Exchange processes of volatile organic compounds above a tropical rainforest: Implications for modeling tropospheric chemistry above dense vegetation. *J. Geophysical Research: Atmospheres* 109, D18306. doi: 10.1029/2004jd004738

Kesselmeier, J., Kuhn, U., Rottenberger, S., Biesenthal, T., Wolf, A., Schebeske, G., et al. (2002). Concentrations and species composition of atmospheric volatile organic compounds (VOCs) as observed during the wet and dry season in Rondonia (Amazonia). *J. Geophysical Research: Atmospheres* 107, LBA-20. doi: 10.1029/2000jd000267

Kesselmeier, J., and Staudt, M. (1999). Biogenic volatile organic compounds (VOC): an overview on emission, physiology and ecology. *J. Atmos. Chem.* 33, 23–88. doi: 10.1023/a:1006127516791

Langford, B., House, E., Valach, A., Hewitt, C. N., Artaxo, P., Barkley, M. P., et al. (2022). Seasonality of isoprene emissions and oxidation products above the remote Amazon. *Environ. Science: Atmospheres* 2, 230–240. doi: 10.1039/d1ea00057h

Langford, B., Misztal, P. K., Nemitz, E., Davison, B., Helfter, C., Pugh, T. A. M., et al. (2010). Fluxes and concentrations of volatile organic compounds from a South-East Asian tropical rainforest. *Atmos. Chem. Phys.* 10, 8391–8412. doi: 10.5194/acp-10-8391-2010

Leuzinger, S., Hartmann, A., and Körner, C. (2011). Water relations of climbing ivy in a temperate forest. *Planta* 233, 1087–1096. doi: 10.1007/s00425-011-1363-6

Lin, M., Malyshev, S., Shevliakova, E., Paulot, F., Horowitz, L. W., Fares, et al. (2019). Sensitivity of ozone dry deposition to ecosystem-atmosphere interactions: A critical appraisal of observations and simulations. *Global Biogeochem. Cycles* 33, 1264–1288. doi: 10.1029/2018gb006157

Liu, Y., Brito, J., Dorris, M. R., Rivera-Rios, J. C., Seco, R., Bates, K. H., et al. (2016). Isoprene photochemistry over the Amazon rainforest. *Proc. Natl. Acad. Sci.* 113, 6125–6130. doi: 10.1073/pnas.1524136113

Liu, Y., El Haddad, I., Scarfogliero, M., Nieto-Gligorovski, L., Temime-Roussel, B., Quivet, E., et al. (2009). In-cloud processes of methacrolein under simulated conditions – Part 1: Aqueous phase photooxidation. *Atmos. Chem. Phys.* 9, 5093–5105. doi: 10.5194/acpd-9-6397-2009

Liu, Y. J., Herdlinger-Blatt, I., McKinney, K. A., and Martin, S. T. (2013). Production of methyl vinyl ketone and methacrolein via the hydroperoxyl pathway of isoprene oxidation. *Atmos. Chem. Phys.* 13, 5715–5730. doi: 10.5194/acp-13-5715-2013

Lovynska, V., Sytntyk, S., Kharytonov, M., Lakyda, P., and Piestova, I. (2018). LAI estimation by direct and indirect methods in Scots pine stands in Northern Steppe of Ukraine. *J. For. Sci.* 64 (12), 514–522. doi: 10.17221/79/2018-JFS

Marais, E. A., Jacob, D. J., Jimenez, J. L., Campuzano-Jost, P., Day, D. A., Hu, W., et al. (2016). Aqueous-phase mechanism for secondary organic aerosol formation from isoprene: application to the southeast United States and co-benefit of SO_2 emission controls. *Atmos. Chem. Phys.* 16, 1603–1618. doi: 10.5194/acp-16-1603-2016

Matsui, K., Sugimoto, K., Mano, J. I., Ozawa, R., and Takabayashi, J. (2012). Differential metabolisms of green leaf volatiles in injured and intact parts of a wounded leaf meet distinct ecophysiological requirements. *PLoS One* 7 (4), e36433. doi: 10.1371/journal.pone.0036433

Miyoshi, A., Hatakeyama, S., and Washida, N. (1994). OH radical-initiated photooxidation of isoprene: An estimate of global CO production. *J. Geophysical Research: Atmospheres* 99, 18779–18787. doi: 10.1029/94JD01334

Montzka, S. A., Trainer, M., Goldan, P. D., Kuster, W. C., and Fehsenfeld, F. C. (1993). Isoprene and its oxidation products, methyl vinyl ketone and methacrolein, in the rural troposphere. *J. Geophysical Research: Atmospheres* 98, 1101–1111. doi: 10.1029/92jd02382

Muramoto, S., Matsubara, Y., Mwenda, C. M., Koeduka, T., Sakami, T., Tani, A., et al. (2015). Glutathionylation and reduction of methacrolein in tomato plants account for its absorption from the vapor phase. *Plant Physiol.* 169, 1744–1754. doi: 10.1104/pp.15.01045

Nemitz, E., Milford, C., and Sutton, M. A. (2001). A two-layer canopy compensation point model for describing bi-directional biosphere-atmosphere exchange of ammonia. *Q. J. R. Meteorolog. Soc* 127, 815–833. doi: 10.1256/smsqj.57305

Nguyen, T. B., Crounse, J. D., Teng, A. P., St. Clair, J. M., Paulot, F., Wolfe, G. M., et al. (2015). Rapid deposition of oxidized biogenic compounds to a temperate forest. *Proc. Natl. Acad. Sci.* 112, E392–E401. doi: 10.1073/pnas.1418702112

Nguyen, T. B., Tyndall, G. S., Crounse, J. D., Teng, A. P., Bates, K. H., Schwantes, R. H., et al (2016). Atmospheric fates of Criegee intermediates in the ozonolysis of isoprene. *Phys. Chem. Chem. Phys.* 18 (15), 10241–10254. doi: 10.1039/c6cp00053c

Niinemets, Ü., Fares, S., Harley, P., and Jardine, K. J. (2014). Bidirectional exchange of biogenic volatiles with vegetation: emission sources, reactions, breakdown and deposition. *Plant Cell Environ.* 37, 1790–1809. doi: 10.1111/pce.12322

Ossola, R., and Farmer, D. K. (2024). The chemical landscape of leaf surfaces and its interaction with the atmosphere. *Chem. Rev.* 124, 5764–5794. doi: 10.1021/acs.chemrev.3c00763

Park, C., Schade, G. W., and Boedeker, I. (2011). Characteristics of the flux of isoprene and its oxidation products in an urban area. *J. Geophys. Res. Atmos.* 116, D21303. doi: 10.1029/2011JD015856

Peeters, J., Muller, J. F., Stavrakou, T., and Nguyen, V. S. (2014). Hydroxyl radical recycling in isoprene oxidation driven by hydrogen bonding and hydrogen tunneling: The upgraded LIM1 mechanism. *J. Phys. Chem. A* 118, 8625–8643. doi: 10.1021/jp5033146

Peeters, J., Nguyen, T. L., and Vereecken, L. (2009). HO x radical regeneration in the oxidation of isoprene. *PCCP* 11, 5935–5939. doi: 10.1039/b908511d

Perring, M. P., De Frenne, P., Hertzog, L. R., Blondeel, H., Depauw, L., Maes, S. L., et al. (2020). Increasing liana frequency in temperate European forest understories is driven by ivy. *Front. Ecol. Environ.* 18, 550–557. doi: 10.1002/fee.2266

Pierotti, D., Wofsy, S. C., Jacob, D., and Rasmussen, R. A. (1990). Isoprene and its oxidation products: Methacrolein and methyl vinyl ketone. *J. Geophys. Res. Atmos.* 95 (D2), 1871–1881. doi: 10.1029/JD095iD02p01871

Popp, C., Burghardt, M., Friedmann, A., and Riederer, M. (2005). Characterization of hydrophilic and lipophilic pathways of Hedera helix L. cuticular membranes: permeation of water and uncharged organic compounds. *J. Exp. Bot.* 56, 2797–2806. doi: 10.1093/jxb/eri272

Pye, H. O., and Seinfeld, J. H. (2010). A global perspective on aerosol from low-volatility organic compounds. *Atmos. Chem. Phys.* 10, 4377–4401. doi: 10.5194/acp-10-4377-2010

Pyhäjärvi, T., Kujala, S. T., and Savolainen, O. (2020). 275 years of forestry meets genomics in Pinus sylvestris. *Evol. Appl.* 13, 11–30. doi: 10.1111/eva.12809

Quiñonez-Piñón, M. R., and Valeo, C. (2019). Scaling approach for estimating stand sapwood area from leaf area index in five boreal species. *Forests* 10, 829. doi: 10.3390/f10100829

Seifried, T. M., Bieber, P., Felgitsch, L., Vlasich, J., Reyzek, F., Schmale, D. G. III, et al (2020). Surfaces of silver birch (*Betula pendula*) are sources of biological ice nuclei: in vivo and in situ investigations. *Biogeosciences* 17 (22), 5655–5667. doi: 10.5194/bg-17-5655-2020

Shutter, J. D., Cox, J. L., and Keutsch, F. N. (2024). Leaf-level bidirectional exchange of formaldehyde on deciduous and evergreen tree saplings. *ACS Earth Space Chem.* 8, 723–733. doi: 10.1021/acsearthspacechem.3c00325

Simpson, D., Benedictow, A., Berge, H., Bergström, R., Emberson, L. D., Fagerli, H., et al. (2012). The EMEP MSC-W chemical transport model–technical description. *Atmos. Chem. Phys.* 12, 7825–7865. doi: 10.5194/acp-12-7825-2012

Skamarock, W. C., Klemp, J. B., Dudhia, J., Gill, D. O., Liu, Z., Berner, J., et al. (2019). "A description of the advanced research WRF version 4 (NCAR tech. Note NCAR/TN-556+STR)," in *National Center for Atmospheric Research*. (Boulder, Colorado: National Center for Atmospheric Research). doi: 10.5065/1dfh-6p97

Skiba, U., Medinets, S., Cardenas, L. M., Carnell, E. J., Hutchings, N. J., and Amon, B. (2021). Assessing the contribution of soil NO_x emissions to European atmospheric pollution. *Environ. Res. Lett.* 16, 025009. doi: 10.1088/1748-9326/abd2f2

Soro, A., Lenz, P., Roussel, J. R., Nadeau, S., Pothier, D., Bousquet, J., et al. (2023). The phenotypic and genetic effects of drought-induced stress on wood specific conductivity and anatomical properties in white spruce seedlings, and relationships with growth and wood density. *Front. Plant Sci.* 14, 1297314. doi: 10.3389/fpls.2023.1297314

Spirig, C., Neftel, A., Ammann, C., Dommen, J., Grabmer, W., Thielmann, A., et al (2005). Eddy covariance flux measurements of biogenic VOCs during ECHO 2003 using proton transfer reaction mass spectrometry. *Atmos. Chem. Phys.* 5, 465–481. doi: 10.5194/acp-5-465-2005

Sprengnether, M., Demerjian, K. L., Donahue, N. M., and Anderson, J. G. (2002). Product analysis of the OH oxidation of isoprene and 1,3-butadiene in the presence of NO. *J. Geophys. Res. Atmos.* 107 (D15), ACH-8. doi: 10.1029/2001JD000716

Stroud, C. A., Roberts, J. M., Goldan, P. D., Kuster, W. C., Murphy, P. C., Williams, E. J., et al. (2001). Isoprene and its oxidation products, methacrolein and methylvinyl ketone, at an urban forested site during the 1999 Southern Oxidants Study. *J. Geophysical Research: Atmospheres* 106, 8035–8046. doi: 10.1029/2000jd900628

Tani, A., Tobe, S., and Shimizu, S. (2010). Uptake of methacrolein and methyl vinyl ketone by tree saplings and implications for forest atmosphere. *Environ. Sci. Technol.* 44 (18), 7096–7101. doi: 10.1021/es1017569

Urban, J., Ingwers, M. W., McGuire, M. A., and Teskey, R. O. (2017). Increase in leaf temperature opens stomata and decouples net photosynthesis from stomatal conductance in *Pinus taeda* and *Populus deltoides x nigra*. *J. Exp. Bot.* 68, 1757–1767. doi: 10.1093/jxb/erx052

van Caspel, W. E., Simpson, D., Jonson, J. E., Benedictow, A. M. K., Ge, Y., di Sarra, A., et al. (2023). Implementation and evaluation of updated photolysis rates in the EMEP MSC-W chemistry-transport model using Cloud-J v7.3e. *Geosci. Model. Dev.* 16, 7433–7459. doi: 10.5194/gmd-16-7433-2023

Wang, X., Liu, S., Bao, L., Zhang, H., Yuan, S., He, M., et al (2021a). Enhanced uptake of methacrolein at the acidic nanoparticle interface: Adsorption, heterogeneous reaction and impact for the secondary organic aerosol formation. *Sci. Total Environ.* 800, 149532. doi: 10.1016/j.scitotenv.2021.149532

Wang, Y., Zhao, J., Liu, H., Li, Y., Dong, W., and Wu, Y. (2021b). Photooxidation of methacrolein in Fe(III)-oxalate aqueous system and its atmospheric implication. *Adv. Atmos. Sci.* 38 (7), 1252–1263. doi: 10.1007/s00376-021-0415-5

Wesely, M. L. (1989). Parameterization of surface resistances to gaseous dry deposition in regional-scale numerical models*. *Atmos. Environ.* 23, 1293–1304. doi: 10.1016/0004-6981(89)90153-4

Wesely, M. L. (2007). Parameterization of surface resistances to gaseous dry deposition in regional-scale numerical models. *Atmos. Environ.* 41, 52–63. doi: 10.1016/j.atmosenv.2007.10.058

Wong, A. Y., Geddes, J. A., Ducker, J. A., Holmes, C. D., Fares, S., Goldstein, A. H., et al. (2022). New evidence for the importance of non-stomatal pathways in ozone deposition during extreme heat and dry anomalies. *Geophys. Res. Lett.* 49, e2021GL095717. doi: 10.1029/2021gl095717

Worton, D. R., Surratt, J. D., LaFranchi, B. W., Chan, A. W., Zhao, Y., Weber, R. J., et al. (2013). Observational insights into aerosol formation from isoprene. *Environ. Sci. Technol.* 47, 11403–11413. doi: 10.1021/es4011064

Wu, Z., Zhang, L., Walker, J. T., Makar, P. A., Perlinger, J. A., and Wang, X. (2021). Extension of a gaseous dry deposition algorithm to oxidized volatile organic compounds and hydrogen cyanide for application in chemistry transport models. *Geosci. Model Dev.* 14 (8), 5093–5105. doi: 10.5194/gmd-14-5093-2021

Xing, Y., Li, H., Huang, L., Wu, H., Shen, H., and Chen, Z. (2018). The production of formaldehyde and hydroxyacetone in methacrolein photooxidation: New insights into mechanism and effects of water vapor. *J. Environ. Sci.* 66, 1–11. doi: 10.1016/j.jes.2017.05.037

Yáñez-Serrano, A. M., Nölscher, A. C., Williams, J., Wolff, S., Alves, E., Martins, G. A., et al. (2015). Diel and seasonal changes of biogenic volatile organic compounds within and above an Amazonian rainforest. *Atmos. Chem. Phys.* 15, 3359–3378. doi: 10.5194/acp-15-3359-2015

Yoo, M. H., Kwon, Y. J., Son, K. C., and Kays, S. J. (2006). Efficacy of indoor plants for the removal of single and mixed volatile organic pollutants and physiological effects of the volatiles on the plants. *J. Am. Soc. For. Hortic. Sci.* 131, 452–458. doi: 10.21273/JASHS.131.4.452

Yu, K., Goldsmith, G. R., Wang, Y., and Anderegg, W. R. (2019). Phylogenetic and biogeographic controls of plant nighttime stomatal conductance. *New Phytol.* 222, 1778–1788. doi: 10.1111/nph.15755

Zhang, L., Brook, J. R., and Vet, R. (2003). A revised parameterization for gaseous dry deposition in air-quality models. *Atmos. Chem. Phys.* 3, 2067–2082. doi: 10.5194/acp-3-2067-2003

Zhang, L., He, Z., Wu, Z., Macdonald, A. M., Brook, J. R., and Kharol, S. (2023). A database of modeled gridded dry deposition velocities for 45 gaseous species and three particle size ranges across North America. *J. Environ. Sci.* 127, 264–272. doi: 10.1016/j.jes.2022.05.030